Implications of Deformation Following the 2002 Denali, Alaska Earthquake for Postseismic Relaxation Processes and Lithospheric Rheology

Andrew M. Freed[1], Roland Bürgmann[2], Eric Calais[1], Jeff Freymueller[3], and Sigrún Hreinsdóttir[3]

[1]Department of Earth and Atmospheric Sciences, Purdue University, West Lafayette, Indiana, USA
[2]Department of Earth and Planetary Science, University of California Berkeley, Berkeley, California, USA
[3]Geophysical Institute, University of Alaska Fairbanks, Fairbanks, Alaska, USA

Abstract

During the first 2 years following the 2002 M_w = 7.9 Denali, Alaska strike-slip earthquake, a large array of Global Positioning System (GPS) receivers recorded rapid postseismic surface motions extending at least 300 km from the rupture and at rates of more than 100 mm/yr in the near-field. Here we use 3-D viscoelastic finite element models to infer the mechanisms responsible for these postseismic observations. We consider afterslip both from an inversion of GPS displacements and from stress-driven forward models, poroelastic rebound, and viscoelastic flow in the lower crust and upper mantle. Several conclusions can be drawn: (1) No single mechanism can explain the postseismic observations. (2) Significant postseismic flow below a depth of 60 km is required to explain observed far-field motions, best explained by a weak upper mantle with a depth dependent effective viscosity that ranges from > 10^{20} Pa s at the Moho (50 km depth) to 3-4 x10^{18} Pa s at 100 km depth. (3) Shallow afterslip within the upper crust occurs adjacent to and beneath the regions of largest coseismic slip. (4) There is a contribution from deformation in the middle and lower crust from either lower crustal flow or stress-driven slip. Afterslip is preferred over broad viscoelastic flow owing to the existence of seismic velocity discontinuities across the fault at depth, though our modeling does not favor either mechanism. If the process is viscoelastic relaxation, the viscosity is a factor of 3 greater than the inferred mantle viscosity. (5) Poroelastic rebound probably contributed to the observed postseismic deformation in the immediate vicinity of the Denali/Totschunda junction. These conclusions lead us to infer an Alaskan mechanical lithosphere that is about 60 km thick, overlying a weak

asthenosphere, and a Denali fault that cuts through the entire lithosphere with shear accommodated by faulting in the top ~20 km and time-dependent aseismic shear below.

1.0 Introduction

A large earthquake can be utilized as a rock deformation experiment in which sudden stress changes trigger an observable postseismic response that reveals rheological properties of the lithosphere. We use such experiments to clarify the relative contributions of various postseismic mechanisms, the depth at which they operate, and the nature of the strain rate-to-stress relationship (e.g., linear versus non-linear). In order for such experiments to be successful–where success is measured as the ability to infer a unique mechanical explanation for the postseismic deformation–postseismic observations must be dense enough to reveal surface deformation patterns and measured often enough to characterize the time dependence of postseismic transients. In addition, the earthquake must be large enough to impart stress to a broad and deep region of the lithosphere. The November 3, 2002, M_w = 7.9 Denali, Alaska earthquake is the largest strike-slip event to be observed with a reasonably large array of GPS instruments, making it one of the most promising large scale rock deformation experiments with which to explore and understand the response of the Earth's lithosphere to loading.

The Denali earthquake ruptured along three fault segments: the previously unrecognized Susitna Glacier thrust fault and the right-lateral Denali and Totschunda strike-slip faults (Figure 1) [Eberhart-Phillips et al., 2003a]. The Susitna Glacier fault may be part of a thrust system that contributes to uplift of the Alaska Range (including Denali) and may merge with the Denali fault at depth [Ridgway et al., 2002]. The Denali fault, comprising the bulk of the rupture surface, is an active intraplate strike-slip fault that accommodates shear strain associated with the oblique subduction of the Pacific plate and collision of the Yakutat block on the southern margin of Alaska [Plafker et al., 1994]. The Totschunda fault splays off of the Denali fault to the southeast, and may be part of a developing connection between the plate-bounding Queen Charlotte-Fairweather and western Denali faults [Richter and Matson, 1971].

The Denali fault earthquake had 340 km of surface rupture and was the largest strike-slip earthquake in North America in almost 150 years [Eberhart-Phillips et al., 2003a]. Following the earthquake, postseismic deformation was observed more than 300 km away from the fault, with rates near the fault measured at more than 100 mm/yr for the first six months, and significant surface deformation well in excess of interseismic rates continues to be observed more than two years after the earthquake. Measurement of these deformations became an immediate scientific priority soon after the earthquake, as they provide constraints from which to infer the rheology of the Alaskan lithosphere and evolution of stress in the aftermath of the Denali fault earthquake.

Understanding the mechanical strength (rheology) of the lithosphere and the processes that govern postseismic stress transfer is central to our understanding of the earthquake cycle and seismic hazards. Earthquakes do not simply release built-up stress, they redistribute it—a process that greatly influences regional seismicity, sometimes inducing earthquake sequences, other times ushering in periods of seismic quiescence [see reviews by Stein, 1999, 2003; King and Cocco, 2001; Freed, 2005]. Postseismic processes induce a further evolution of crustal stresses, leading to earthquake triggering long after aftershock activity has died down [Pollitz and Sacks, 1995, 1997, 2002; Pollitz et al., 1998a; Freed and Lin, 1998, 2001, 2002; Nostro et al., 2001; Zeng, 2001; Chéry et al., 2001; Hearn et al., 2002; Vergnolle et al., 2003; Casarotti and Piersanti, 2003]. On a more fundamental level, inferences from postseismic studies provide insights into some of the most basic properties of the lithosphere, such as the constitutive properties and extent of faulting, the permeability of the crust and influence of fluid flow, the depth extent of the elastic portion of the crust, and the relative viscoelastic strength of the lower crust and upper mantle, all of which influence how mantle convection manifests itself as plate tectonics.

Three primary mechanisms of stress relaxation are thought to be initiated following large earthquakes: afterslip, poroelastic rebound, and viscoelastic flow. Afterslip is the process by which coseismic stress changes cause aseismic slip following the earthquake [e.g., Marone et al., 1991]. Such slip can occur within the rupture surface, on a nearby

fault surface that did not break in the event, or on a down-dip extension of the fault, where slip generally occurs aseismically because of high pressures and warmer temperatures. Based on postseismic observations, afterslip has been inferred to be an important mechanism following a number of earthquakes [Savage and Church, 1974; Buckman et al., 1978; Segall et al., 2000; Heki et al., 1997; Hsu et al., 2002; Bürgmann et al., 2002; Hearn et al., 2002; Jacobs et al., 2002; Kenner and Segall, 2003; Savage et al., 2003]. Poroelastic rebound occurs when coseismic stresses produce excess fluid pressure in the near-field region (usually within 10-30 km from the fault). This pressure change drives fluid flow, inducing postseismic deformation and stress changes [Booker, 1974; Rice and Cleary, 1976; Peltzer et al., 1996; Bosl and Nur, 2002; Masterlark and Wang, 2002; Jónsson et al., 2003]. Viscoelastic relaxation arises from the inability of the hot (and therefore weaker) lower crust and/or upper mantle to sustain imparted coseismic stress changes. On the time scale of an earthquake rupture (tens of seconds), the entire lithosphere responds to the earthquake in an elastic manner. However, coseismic stress changes cannot be sustained in these hot, deeper regions and they relax viscously in the years to decades following the earthquake. This induces a transfer of stress both laterally and upward to the shallow seismogenic crust, causing observable postseismic surface deformations [Nur and Mavko, 1974; Thatcher et al., 1980; Savage and Prescott, 1981; Ivins, 1996; Deng et al., 1998; Pollitz et al., 2000, 2001; Freed and Bürgmann, 2004].

A major problem in understanding the postseismic response of the lithosphere to an earthquake is one of uniqueness. Savage [1990] showed that for an infinitely long, strike-slip earthquake with uniform coseismic slip, postseismic deformation due to viscoelastic relaxation of an asthenospheric half-space can be reproduced by a properly chosen afterslip model. This ambiguity diminishes for finite ruptures, but limitations in spatial and temporal coverage of 3D postseismic deformation still make the convergence to a unique postseismic model a difficult undertaking [e.g., Hearn, 2003]. To illustrate the difficulty, consider the range of conclusions drawn from postseismic analysis of the 1992 Landers earthquake. Several authors inferred only afterslip [Shen et al., 1994; Bock et al., 1997; Savage and Svarc, 1997], only viscoelastic relaxation [Deng et al., 1998; Pollitz et al., 2000; Freed and Bürgmann, 2004], a combination of poroelastic rebound and

afterslip [Peltzer et al., 1998; Fialko, 2004], or a combination of poroelastic rebound and viscoelastic relaxation [Masterlark and Wang, 2002]. Though different spatial and temporal scales are considered in these studies, many of the conclusions regarding the primary active mechanisms are in conflict.

Rich GPS coverage of postseismic deformation following the 2002 Denali earthquake provides a data set from which to draw some robust conclusions regarding the contribution of the various candidate mechanisms and develop a mechanical model of the Alaskan lithosphere. Using 19 months of data from 15 stations, Pollitz [2005] finds that postseismic deformation is dominated by transient relaxation in the upper mantle. In contrast to our study, Pollitz (2005) did not consider afterslip or poroelastic rebound in his modeling, but did consider a wider range of viscoelastic rheologies. In this study we address the contribution of the candidate mechanisms to the total surface deformation at the continuous sites and some of the campaign sites for the first 2 years following the earthquake. We leave the interpretation of transient time-series (and questions of linear versus non-linear viscosity) to a companion study.

2.0 Postseismic Observational Constraints

2.1 Deployment Considerations

The Denali earthquake occurred in the middle of a pre-existing network of campaign GPS sites, with known pre-earthquake velocities [Fletcher, 2002]. Within hours of the earthquake, we initiated a field response with GPS measurements at some of those sites. In addition to the campaign measurements, 10 new continuous sites were installed within 2 weeks after the earthquake in the areas potentially affected by postseismic deformation (Figure 1). Eight of these sites were instrumented with Trimble 5700 receivers with Zephyr Geodetic antennas, and two with Ashtech Micro-Z receivers with choke ring antennas. All of these sites used a single vertical rod for monumentation, generally 2” diameter stainless steel or invar. These new sites added to 7 existing continuous sites that were operating in central Alaska at the time of the earthquake.

As our focus is on distinguishing processes in the deep fault zone and the lower crust and upper mantle, we required sites at a wide range of distances from the rupture, including some more than 100 km away. Preliminary models with different rheologies allowed us to determine regions where surface deformation data would provide optimal information to constrain rheological model parameters. We also drew on the work of Hearn et al. [2002] for added insight. These studies showed that the optimal network design changes depending on the assumed deformation mechanism and its constitutive parameters, and evolves with time. However, it is always important to include sites located adjacent to the fault ends, as well as across the center of the fault. Also, sites should be spaced relatively closely at short distances (15-50 km) from the fault. In addition to science criteria, we selected continuous sites also on the basis of (1) their accessibility in winter (for maintenance and data download), (2) the availability of bedrock, (3) the absence of land-use restrictions, and (4) prior observation history, if possible.

During the summer of 2003, five additional continuous sites were installed (equipped with Trimble 5700 units), the two Ashtech units were replaced by Trimble 5700s and Zephyr Geodetic antennas, and bracing rods were added to the monuments. Before and after survey ties showed no evidence for horizontal offsets associated with the monumentation changes. Data are downloaded manually every 4-8 weeks and uploaded to the UNAVCO archive where they are made publicly available (www.unavco.org). Five of the new CGPS sites installed after the Denali earthquake are now incorporated in the Plate Boundary Observatory (PBO, pbo.unavco.org). During the summer of 2004, the receivers at these sites were replaced by Trimble Net-RS receivers and choke ring antennas. Unfortunately, this meant that at some sites there were two antenna changes in the time series. We estimated the corresponding offsets and corrected for them in the time series. The USGS also installed 4 semi-continuous sites in the vicinity of the rupture that are intended to be observed twice a year for a few weeks at a time. These sites are included in the present study. In addition to continuous GPS measurements, we have performed six measurement campaigns between 2002 and 2005 at about 100 sites

distributed over the area potentially affected by postseismic deformation. Campaign sites were typically observed during 48 to 72 hour sessions.

2.2 Data Processing

Phase and pseudorange GPS data were processed in single-day solutions using the GAMIT software (version 10.2; King and Bock, 2005). Comparable solutions were obtained using the GIPSY-OASIS software. We solved for regional station coordinates, satellite state vectors, 7 tropospheric zenith delay parameters per site and day, and phase ambiguities using doubly-differenced GPS phase measurements. We used IGS final orbits, IERS earth orientation parameters, and applied azimuth and elevation dependent antenna phase center models, following the tables recommended by the IGS. We included 10 global IGS stations in North America to serve as ties with the terrestrial reference frame (ITRF2000; Altamimi et al., 2002).

The least squares adjustment vector and its corresponding variance-covariance matrix for station positions and orbital elements estimated for each independent daily solution were then combined with global SINEX (Solution Independent Exchange format) files from the IGS daily processing routinely done at the Scripps Orbital and Permanent Array Center (http://sopac.ucsd.edu). The reference frame is implemented using this unconstrained combined solution by minimizing the position and velocity deviations of 41 IGS core stations with respect to the ITRF2000 while estimating an orientation, translation and scale transformation. In this process, height coordinates were downweighted using a variance scaling factor of 10 compared to the horizontal components. The large spatial extent of postseismic deformation, the widespread tectonic activity in Alaska, and the large dimensions of the study area impose that we map horizontal displacements with respect to stable North America rather than to a fixed site. To do so, we corrected site positions for the America/ITRF2000 angular rotation given by Calais et al. [2003].

2.3 Time Series Modeling

For the purpose of the present study, we are interested in the cumulative surface deformation for the two-year period following the 2002 earthquake (Nov. 2002 thru Nov. 2004). Using two complete years enables us to estimate and remove annual and semiannual signals within the GPS data. To do so, we model site positions as the sum of (1) a linear term representing secular elastic strain accumulation, (2) a logarithmic term representing postseismic deformation, (3) an annual and semi-annual periodic term representing seasonal effects not modeled in the GPS data analysis, and (4) DC offsets due to equipment changes or problems at the site. The model equation is:

$$y = at + b + \sum_{i=1}^{n} c_i H_i(t) + d\sin(2\pi t) + e\sin(2\pi t) + f\sin(4\pi t) + g\sin(4\pi t) + h\ln(1 + t/\tau) \quad (1)$$

where a, b, c_i, d, e, f, g, h, and τ are estimated by inverting the site position data y using a singular value decomposition scheme. $H_i(t)$ is a binary operator equal to 0 or 1 before or after offset i, respectively. The logarithmic term in equation (1) is a convenient means of parameterizing time-dependent postseismic deformation. Although the data is well fit by this model, we do not ascribe a physical significance to the estimated model parameters or predictive power to the overall model. We use this approach only as a curve-fitting convenience to remove non-tectonic effects (seasonal variations and DC offsets) and estimate displacement uncertainties. One-sigma uncertainties on cumulative displacements are taken as the RMS of the scatter of the position data about the model presented above. After estimating all of the above terms, we remove the DC offsets and annual and semi-annual terms, keeping the secular and logarithmic terms as the constraint set for our postseismic study. This process is illustrated in Figure 2 for data recorded at station MENT.

2.4 GPS Results

The observed postseismic horizontal surface displacements of 14 continuous and 27 campaign stations for the two-year period following the Denali earthquake are shown in Figure 3 and listed in Table 1. Uncertainties shown for cumulative displacements in Figure 3 are two-sigma (95% confidence level). The typical displacement uncertainty is

6 and 5 mm in the east and north components for continuous stations, and 10 and 9 mm for the campaign stations. We limit the stations used in this study to be north of a latitude of 62°N (Figure 1). As discussed below, stations south of this latitude are affected by elastic strain associated with the subduction zone, which is not considered in the current model. For campaign observations we only considered sites where measurements were made within 1 month of the Denali earthquake and within 2 months of the end of the two-year period of interest, otherwise the extraction of the total displacement was prone to extrapolation errors.

The pattern of displacements shown in Figure 3 represents a classical observed transient response to strike-slip earthquakes [e.g., Reilinger et al., 2000; Hudnut et al., 2002; Savage et al., 2003]; namely, continued shear motion greatly accelerated compared to prequake velocities. For the 2-year period following the earthquake, postseismic displacements in the near-field (within 50 km of the fault) reach 200 mm. They remain significant (up to 20-30 mm) at distances of 100-200 km from the fault and decay to less than 10 mm about 300 km north of the rupture. A key challenge is to identify candidate postseismic mechanisms that can explain both the near- and far-field observations.

Observed vertical postseismic displacements have a relatively low signal-to-noise ratio and show very large seasonal signals (Figure 2c), making it difficult to differentiate tectonic from non-tectonic contributions. We were unable to reliably identify and remove non-tectonic deformation from campaign GPS, and thus we do not consider vertical motions of campaign sites at this time. Though we were able to extract a vertical tectonic signal from the continuous GPS time-series, the uncertainties combined with high seasonal variations leave us suspicious of these results as well. Additional data to identify the seasonal deformation signal will be required to make full use of the vertical displacements. Furthermore, without reliable campaign measurements it is difficult to infer the regional uplift and subsidence pattern associated with postseismic deformation. This is unfortunate, as such information would have served as a powerful constraint on postseismic models [e.g., Pollitz et al., 2000; Hearn, 2003]. We therefore do not use the vertical displacement data as a constraint in our formal assessment of candidate models.

However, we calculate vertical displacements from models derived using horizontal constraints, then compare these results with continuous GPS vertical observations. Vertical displacement estimates for the continuous GPS stations are shown in the inset of Figure 3. The main feature of the vertical displacement field from continuous GPS data is a significant uplift near the junction of the Denali and Totschunda faults. This uplift signal is clearly seen in the time series (Figure 2c), although the uncertainty in the rate remains high. It is also clear that sites far from the rupture did not experience rapid uplift after the earthquake.

3.0 Analysis Approach

Our objective is it to determine, as uniquely as possible, the mechanical processes responsible for the observed postseismic surface deformation following the 2002 Denali earthquake. The analysis requires several steps: determine long-term surface deformation due to regional tectonics of southern Alaska that will be present within the postseismic data, determine coseismic stress changes associated with the Denali rupture that drive postseismic processes, and determine the various contributions of candidate mechanisms (viscoelastic relaxation, poroelastic rebound, and afterslip) to postseismic surface deformations.

The analysis is accomplished by developing pre-, co-, and postseismic finite element models of the Denali earthquake and the surrounding region. The finite element mesh used throughout was developed using the software "I-deas" (www.eds.com) and is shown in Figure 4. The finite element models are used for all phases of the analysis except for the afterslip inversions. This code has been successfully used in several previous postseismic studies [Freed and Lin, 2001, 2002; Freed and Bürgmann, 2004]. The 3-D mesh takes on a half cylinder shape to accommodate block motion in southern Alaska (discussed in the next section). Faults are modeled by generating discontinuities in the mesh on which the specified slip or slip rate is imposed. Coseismic slip and block rotation rates are prescribed as opposed to determined from a response to driving stresses. However, we do explore stress driven postseismic afterslip on a frictionless down-dip extension of the Denali fault. The following sections describe the regional tectonics and

boundary conditions assumed, the development of the coseismic model that drives the postseismic response, and the approach of modeling each candidate postseismic mechanism. We consider each mechanism separately and in combinations. Models are assessed by comparison of calculated horizontal surface deformations to GPS observations.

4.0 Pre-Denali Quake Kinematics and Boundary Conditions

The curvature of the Denali fault can be approximated by a small circle which bounds a rotating circular block centered near the coast of southern Alaska [Stout and Chase, 1980; Lahr and Plafker, 1980; Fletcher, 2002]. We found that a small circle centered at 60.0 ºN 147.7 ºW provides a good fit for the ~350 km length of the fault that ruptured in 2003. Pre-Denali earthquake GPS velocities suggest that the semi-circular block defined by the Denali fault is rotating counter-clockwise with respect to stable North America (black arrows in Figure 5) [Fletcher, 2002]. There are two GPS profiles across the Denali fault at about 146°W and 150°W. The eastern profile shows 6 ± 1 mm/yr of right-lateral shear across the Denali fault, but lacks sites close to the fault. The western profile shows a higher rate, 8 ± 1 mm/yr, but features a broad and asymmetric 50-km-wide region of right-lateral shear. Fletcher [2002] suggested that the Denali fault system at this longitude consisted of two active strands, with one located north of the fault trace that ruptured in 2002. Because both profiles show velocities parallel to the curving Denali fault, Fletcher [2002] followed Lahr and Plafker [1980] and proposed that the southern Alaska block south of the Denali and Totschunda faults rotates counter-clockwise relative to North America; using a 3D dislocation model the best-fitting block rotation velocity is 0.77°/My.

It is important to reasonably model prequake tectonics in postseismic studies for two reasons. The first is that postseismic surface deformation contains a component of secular regional deformation that must be accounted for. The second is that when we consider stress-dependent rheologies (in a companion study), the total stress, not just coseismic stress changes, becomes important [Freed and Bürgmann, 2004]. These factors led us to develop the half-cylinder model geometry, which enables us to simulate the

rotation of the block bounded by the Denali fault. This is accomplished by first introducing a lithospheric fault along the small-circle boundary that completely cuts through the model (along the dashed line in Figure 4c), then applying a rotational velocity boundary condition with an angular velocity of 0.77°/million years to match the long term Denali fault slip rate [Fletcher, 2002]. The lithospheric fault serves to enable rotation of the circular inner block with respect to the outer cylinder, which is fixed on all side and bottom boundaries. We prevent the fault from slipping from the surface to a locking depth, the depth of which controls the width of the elastic strain accumulation zone. We find that a locking depth of ~24 km leads to the approximately 50-km-wide strain accumulation zone across the Denali fault observed in GPS measurements. This is consistent with the locking depth of 28 ± 8 km inferred by Fletcher [2002] if a single fault model is assumed. Fletcher [2002] infers about half that locking depth if slip is partitioned between the Denali and Hines Creek faults, but we do not consider such complexity in this model, and this simplification does not affect the results of the present paper.

Surface displacements predicted by our prequake model reasonably match the observed fault-parallel velocities in the vicinity of the Denali fault (Figure 5). Our model does not explain the large northerly velocity component observed at stations GNAA and TAZL to the south, which we assume arises due to elastic strain accumulation on the subduction zone to the south [Sauber et al., 1997; Zweck et al., 2002]. Future models should incorporate the influence of subduction on the region between the plate boundary and the Denali fault, but that complexity is beyond the scope of the present work. We thus make no attempt in our analysis to match postseismic surface velocities south of 62° latitude. Because we do not consider strain accumulation due to subduction in our model, we simply remove this component of deformation at stations GNAA and TAZL from our postseismic constraints. This is accomplished by estimating the rate due to the subduction component as the difference between the observed preseismic velocities and that of our block model, then subtracting that deformation from the postseismic data for these two stations. This correction has been applied to the observed displacements shown in all corresponding figures and Table 1. Our prequake model also does not explain the

southerly velocity component observed at station HURR, which is influenced by postseismic effects associated with the 1964 Alaska earthquake, and by a 1998-2001 slow slip event on the subduction interface [Fletcher, 2002; Zweck et al., 2002; Freymueller et al., 2002; Ohta et al., in prep]. This southward motion does not appear to be present in the post-Denali observations, and we do not attempt to correct for this component.

5.0 Coseismic Slip

Coseismic slip induces a sudden change in stress to which postseismic mechanisms respond, and thus represents a critical component for the postseismic model. Two primary factors influence the coseismic stress change: the coseismic slip distribution and the elastic structure of the surrounding lithosphere. The 2002 Denali earthquake began as a thrusting event on the Susitna Glacier fault (Figure 1), on a north dipping rupture plane that dips 25° near the surface (top 2 km), then 48° to a depth of about 10 km, where it comes in contact with (or is close to) the Denali fault [Eberhart-Phillips et al., 2003a]. Slip then jumped to the nearly vertical Denali fault, producing predominately right-lateral slip for about 220 km, before jumping to the Totschunda fault where right-lateral slip continued for another 30 km. A detailed coseismic slip distribution has been inferred by Hreinsdottir et al. [2005] from inversion of 232 GPS-measured displacements using an elastic half-space model (Figure 6, color contoured portion). Coseismic slip is characterized by a complex, right-lateral, strike-slip motion with a moderate amount of vertical dip-slip displacement (north-side up). Slip magnitudes on the Denali fault increase from west to east with four localized high-slip patches (> 7 m slip) that extend to a depth of ~18 km. Slip on the Totschunda fault ranges from 1-3 m with the majority being shallower than 9 km depth. These slip estimates are generally consistent with those inferred from other geodetic [Wright et al., 2004], seismic [Ozacar and Beck, 2004], and combined GPS and seismic [Dreger et al., 2004; Oglesby et al., 2004] inversions in terms of the general location of high-slip patches. However, the Hreinsdottir et al. [2005] analysis incorporates substantially more GPS data and a more realistic fault geometry, and has a higher resolution for the static displacements than any other model available.

An interesting feature of the coseismic slip distribution is the area of very low deep slip from about 65-80 in Figure 6, which is adjacent to an area of very high deep slip centered at about 87 km from the hypocenter. Hreinsdóttir et al. [2005] did a variety of simulations, which showed that the model resolution is quite good in that part of the model, and inversion of synthetic data sets and Monte Carlo simulations suggested that such structures (there is a similar feature near the Denali-Totschunda junction) are likely a real feature of the slip distribution. They suggest that these features may be related to the rupture passing through a releasing bend (kink) in the rupture geometry.

Detailed features of the inferred coseismic slip distribution, such as the juxtaposition of low and high slip patches, do not significantly influence our postseismic results. This is because our postseismic viscous and stress-driven deep afterslip models infer flow below 40 km depth, and the intervening crust acts to smooth the distribution of stress at depth. Shallow afterslip models are derived from inversion of the GPS data, so these are not influenced by a calculated coseismic stress distribution. Poroelastic models are the most susceptible to changes in localized coseismic stress distributions, but this mechanism produces small postseismic displacements compared to the other mechanisms considered. In general, we found that as long as the overall slip distribution did not change dramatically (i.e., shifting high slip patches more than 10 km), our results were not influenced by the finer detail of inferred coseismic stress changes.

The elastic structure of southern Alaska has been inferred from seismic refraction velocities and seismic tomography [Eberhart-Phillips, 2003b]. The distribution of shear modulus at various depths derived from the seismic velocities is shown in Figure 7. This inferred structure is suggestive of the mechanics of the Alaskan lithosphere in several respects. First, the inferred elastic structure suggests discontinuities across the Denali fault to depths of at least 65 km. Discontinuities across the trace of the Denali fault are especially noticeable in the contour maps for 33, 48 , and 65 km depth in Figure 7. This is not surprising, because the Denali fault forms the boundary between the Yukon-Tanana terrain to the north and the Wrangellia composite terrain to the south, and offsets rocks of different origin at all levels of the crust. These observed discontinuities imply that shear

within the lower crust and uppermost mantle is localized in a narrow zone that is relatively weak compared to the surrounding regions. This suggests that we should not expect significant broad viscoelastic flow in rock above 65 km depth in the short 2 yr time period of the postseismic observations, although we may expect deformation within a narrow shear zone to this depth. Such an inference, albeit indirect, can be used to discriminate between competing postseismic models.

Second, the elastic strength of the Alaskan lithosphere increases continuously with depth. Figure 8 shows the depth-dependent average elastic strength of the southern Alaska lithosphere inferred from the detailed tomographic structure. Brocher et al. [2004] suggest a Moho depth of about 50 km beneath the Denali fault, shallowing to the north. This would approximately correspond to the jump in shear modulus from 57 to 67 GPa (v_p from 7.5 to 8.0 km/s) at 48-km-depth in Figure 8. We use 50 km as the thickness of the crust in our postseismic analysis. This layered earth model, including the detailed structure shown in Figure 7, forms the basis for the elastic structure we utilize in our coseismic and postseismic models. The Poisson ratio is assumed to be 0.26 throughout based on seismic velocity ratios [Eberhart-Phillips, 2003b]. It is the strong depth dependence of elastic strength that we find to have a significant influence on our postseismic results. As with the coseismic stress distribution, the detailed structure of the elastic model does not significantly influence postseismic model results, as the influence of such structure is smoothed by intervening crust when studying the response of broad regions of the lithosphere to coseismic loading.

The layered Earth model is in obvious conflict with the half-space assumption considered in the inversion for coseismic slip by Hreinsdottir et al. [2005]. Hearn and Bürgmann [2005] find that half-space inversions tend to underestimate seismic moment and slip at depth, and coseismic stresses in the lower crust can be underestimated by a factor of 3, which would have consequences in the modeled response of postseismic processes operating in the lower crust. We find that if we use the slip distribution as described by Hreinsdottir et al. (colored contour portions in Figure 6) in our heterogeneous earth model, we underpredict coseismic surface displacements by about

10% near the fault (within 10 km) to more than 30% at distances of 100 km from the fault (Figure 9b). This problem is rectified by adding additional deep slip to the Hreinsdottir et al. distribution. From forward modeling, we find that we can better match observed coseismic surface displacements by extending slip from 18 to a depth of 24 km. This extension is shown as continued slip contours (no color) in Figure 6. The deepening of the slip distribution also allows us to taper the slip to zero at 24 km (albeit a sharp taper in some cases), which is required to model slip in the continuum of the finite element mesh. A comparison between observed and our layered-earth calculated coseismic surface displacements using the deeper slip model shows good agreement (Figure 9). The added deep slip in the layered model reduces the rms error from 61 to 52 mm, which is comparable to the misfit found by Hreinsdottir et al. using the shallower slip structure in their half-space model. The rms error is calculated as,

$$rms = \left\{ \frac{1}{N} \sum_{1}^{N} \left[\left(obs_i - \mathrm{model}_i \right)^2 \right] \right\}^{1/2} \qquad (2)$$

where obs_i and $model_i$ are the observed and calculated 2-yr cumulative displacements in the north and east directions at each GPS station and N is the total number of cumulative observations.

6.0 Postseismic Deformation Processes

Note that for model comparisons we calculated displacements due to two years of southern block rotation (Figure 10a), then removed this component (together with the subduction related motions of stations GNAA and TAZL) from the observed data set in order to isolate and compare displacements associated with postseismic transients only.

6.1 Poroelastic Rebound

Poroelastic rebound occurs when coseismic induced regions of compression and dilatation in the shallow crust around the fault drive pore fluid flow. Because earthquakes occur over very short time spans, there is essentially no fluid flow immediately after the rupture, when conditions are said to be “undrained”. In time,

pressure gradients drive flow toward a "drained" condition in which fluid pressure equilibrium is reestablished. Under either condition, the constitutive relation between stress and strain is indistinguishable from that of an ordinary elastic material, provided that appropriate values of shear modulus and Poisson's ratio are used [Roeloffs, 1996]. Both conditions can be described using the same shear modulus, requiring only a variation in Poisson's ratio [Roeloffs, 1996]. Laboratory observations indicate that the undrained (coseismic) Poisson ratio of porous media is always larger than the drained (postseismic) Poisson ratio [e.g. Rice and Cleary, 1976]. Consequently, we can model the drained condition simply by reducing the Poisson's ratio used in the coseismic model. The influence of poroelastic rebound is then found by taking the difference in predicted surface deformation between the drained and undrained models [e.g., Peltzer et al., 1996; Jónsson et al., 2003]. Previous analyses of poroelastic rebound suggest that the majority of the process should be completed within a matter of months after the earthquake [e.g., Peltzer et al., 1996, 1998; Masterlark and Wang, 2002; Jónsson et al., 2003]. We therefore assume that the process of poroelastic rebound is completed within the 2-year time period of our study.

Previous analysis following the 1992 Landers quake found that an observed component of postseismic surface deformation could be explained by poroelastic rebound by modeling the drained condition using a reduction in Poisson's ratio from the undrained condition of ~13% (from 0.31 to 0.27) to a depth of 15 km in the crust [Peltzer et al., 1996, 1998]. Using a similar reduction of Poisson's ratio in our Denali model (from 0.26 to 0.22) leads to postseismic surface displacements significantly smaller than those observed in the near-field, and non-existent in the far-field [Figure 10b]. The rms misfit for the poroelastic rebound model is 55 mm – a very poor fit compared to other models. We find that even if we double the reduction in Poisson's ratio used to calculate poroelastic rebound, it would still not begin to explain the observed horizontal displacements. Further decrease of the Poisson ratio would deviate from typical rock properties observed in the laboratory [Rice and Cleary, 1976]. The relatively small inferred contribution of poroelastic rebound to postseismic deformation is due to a relatively small volumetric change induced by the earthquake, as most of the rupture

surface is continuous. The location of the largest postseismic displacements induced by poroelastic rebound are found near the Denali/Totschunda junction, a kink in the rupture surface that produces the largest volumetric strains.

6.2 Lower Crustal Flow

We consider a lower crust that extends from 15-km-depth (the maximum depth of aftershocks) to 50-km-depth (the depth of the inferred Moho). We evaluate a variety of viscosity structures including a uniform viscosity with depth and models in which the viscosity decreases by 1, 2, 3, and 4 orders of magnitude from 15 to 50 km depth (Figure 11a). This suite of models allows us to explore the influence of both the average and depth dependent viscosity structure within the lower crust. The wide range of viscosity structures considered spans relaxation (Maxwell) times (viscosity/shear modulus) from weeks to decades. This large range reflects the great uncertainty in viscosity structure associated with a lack of knowledge regarding mineralogy, temperature, and water fugacity of the Alaskan lower crust, plus uncertainties in how laboratory derived flow laws (e.g. Kirby and Kronenberg, 1987) scale to the field. All lower crustal flow models assume an elastic upper crust and mantle. In the multi-mechanism models we consider below, we will examine evidence for flow in both the lower crust and upper mantle.

The rms misfit was calculated for each lower crustal rheology considered and plotted as a function of viscosity at the base of the lower crust (50 km depth) in Figure 11c. The best fitting model came from the set in which the viscosity varied by 4 orders of magnitude with depth, with a viscosity of 1.5×10^{22} Pa s at 15 km depth (essentially elastic at the time scales considered) to a viscosity of 1.5×10^{18} Pa s at 50 km depth. This model confines lower crustal flow to between ~30 and 50 km depth, with the greatest flow near the base. Such a model follows naturally if viscosity is strongly temperature dependent, as suggested by laboratory experiments [e.g., Kirby and Kronenberg, 1987]. That significant flow is not inferred in the middle crust is consistent with the velocity model of Brocher et al. [2004], which indicates a nearly vertical, discrete fault zone to at least a depth of 30 km.

Calculated surface displacements associated with the best-fitting, lower crustal flow model are compared to observed displacements in Figure 10c. As shown in this figure, with an rms misfit of 28 mm even the best lower crustal flow model does not provide a good fit to the observed horizontal surface displacements. One of the main reasons for the relatively poor fit of a lower crustal flow model is the inability to simultaneously match near- and far-field displacements. Note how the best fitting model (Figure 10c) underestimates far-field displacements. If the model that best matched far-field displacements were shown, many near-field displacements would be over-estimated by more than 50%. In addition, many of the azimuths of the lower crustal flow model displacements are systematically biased between 20° and 30° counter-clockwise in regions south and southeast of the fault, and a similar amount clockwise to the north and northeast regions of the fault. Figure 11d shows rms misfits for far-field (11 stations at ≥100 km from the fault) displacements only. While the overall best-fitting model had a basal viscosity of 1.5×10^{18} Pa s (black line in Figure 11c), the best-fitting far-field model has a basal viscosity of 7×10^{17} Pa s (black line in Figure 11d). While this reduction in viscosity improves the far-field fit, the overall misfit becomes very large. As discussed previously, the seismic velocity structure (Figure 7) suggests that the Denali fault may cut as deep as 60-65 km. This would be consistent with our inability to find a distributed lower crustal flow model consistent with all of the postseismic observations.

6.3 Upper Mantle Flow

Similar to the lower crustal flow study, we considered a variety of viscosity structures for the upper mantle, which we consider to extend from the Moho at 50 km depth to the bottom of the model at a depth of 240 km. However, because of the dissipation of coseismic stresses with depth, mantle below a depth of about 110-120 km is not significantly stressed by the Denali rupture. Thus, postseismic surface deformations are not sensitive to the rheology below this depth. We considered models of uniform viscosity with depth and models in which the viscosity varied by 1, 2, 3, and 4 orders of magnitude from 50 to 120 km depth (Figure 11b). All upper mantle flow models assume an elastic crust to a depth of 50 km.

The rms error was calculated for each rheology considered and plotted as a function of viscosity at 120 km depth in Figure 11e. The best-fitting mantle flow model has an rms value of 32 mm, a slightly greater misfit than the best lower crustal flow model – still not a very good fit to the data. The reason for this misfit is that the mantle flow model cannot fit the magnitude of displacement in the near-field without greatly overshooting displacements in the far-field – opposite to the situation of the lower crustal flow model. However, if we target just the far-field displacements (≥100 km) for minimum misfit (Figure 11f), we can find a model that matches well the far-field displacements while underpredicting the near field. The azimuths of the calculated displacements for the mantle flow model in the near field are systematically misfit for the sites in the central part of the rupture (Figure 10d), counter-clockwise between 10° and 20° to the south of the fault and a similar clockwise rotation to the north of the fault.

The best far-field fitting model, which has a misfit of only 6 mm to the 11 far-field sites, comes from the suite of models in which viscosity decreases by 2 orders of magnitude, from 2 $\times 10^{20}$ Pa s at 50 km depth to 2 $\times 10^{18}$ Pa s at 120 km depth (inset of Figure 10d). As model regions with viscosities above about 2 $\times 10^{19}$ Pa s have minimal influence on postseismic results in a 2-year study, this model essentially consists of a strong mantle lid about 10-15 km thick (from 50 to 60-65 km depth) underlayed by a weak asthenospheric mantle where viscoelastic relaxation becomes significant. Such a model is consistent with the seismic velocity data (presented as elastic stiffness in Figure 7), which suggests that the Denali fault may cut to a depth of 60-65 km. The calculated surface displacements of this model are compared to observed GPS data in Figure 10d. Note the good fit to the far-field data, while near-field displacements are underpredicted. A possible implication is that far-field motions are driven by mantle flow below 60-65 km, with an additional shallow mechanism(s) required to fully explain observed near-field displacements. This problem, along with azimuth errors, will be taken up with the consideration of multiple-mechanism models discussed in Section 6.6.

The relaxation process represented by the best fitting far-field mantle flow model is illustrated in Figure 12, which shows coseismic and postseismic shear stress changes and

the difference between the two. The shear stress change resulting from two years of viscoelastic relaxation alone (Figure 12c) shows a stress decay (blue region) in the upper mantle to a depth of about 120 km. This induces a reloading of the upper crust (yellow region) early in the earthquake cycle.

6.4 Afterslip From GPS Inversion

The assumption that postseismic deformation is the result of afterslip, either within the seismogenic zone or down-dip, can be explored by inverting the GPS observations for an afterslip model that fits the data within their uncertainties. Here we assume that afterslip can be described by a dislocation model of distributed slip in an elastic half-space. In this approach (which is identical to that used in the coseismic slip inversions of Hreinsdottir et al., 2005) we calculate the optimal strike-slip values on a grid of vertical dislocation elements that minimize the misfit (weighted sum of squared residuals) to the GPS data. Positivity constraints (right-lateral strike slip only) and Laplacian smoothing are applied to avoid mechanically implausible and overly rough slip distributions. The model geometry follows the coseismic rupture, but reaches beyond the lateral ends and allows for slip down to 100 km.

The inversion results suggest that observed horizontal surface displacements can be explained by a combination of deep and shallow afterslip, the distribution of which is shown in Figure 13a. This model leads to calculated surface displacements in close agreement to those observed, as shown in Figure 10e. The rms misfit for this afterslip model is 14 mm, representing a good fit to the data for most sites. For far-field sites only, the misfit of the afterslip from inversion model is 5 mm, compared to 6 mm for the upper mantle flow model. Good agreement is not surprising, as the GPS data is the input to an optimization and the inversion is not constrained by physical processes such as coseismic stress changes or coseismically induced changes in friction on the fault. Thus, one must be careful in too freely accepting such a solution as a preferred model simply because of the good fit to the observations.

The inferred deep afterslip shown in Figure 13a is driven by the far-field displacements. The afterslip distribution hugs the 100 km deep boundary of the dislocation model, implying that the inversion wants even deeper slip. A dislocation model with a bottom boundary at only 60 km depth, however, can also satisfy the observational constraints without a significant increase in misfit, though such a model concentrates much of the slip at the very base of the 60 km limit. The solution degrades for models with shallower bottom boundaries, indicating that the inversion is not strongly sensitive to the depth of slip, as long as slip is allowed to occur to at least 60 km depth.

Afterslip inversions also suggest a component of significant shallow afterslip on the eastern part of the Denali fault (at an E-W distance of 180 km in Figure 13a) and a combination of shallow and deep (lower crust) slip on the Totschunda fault. These slip patches are primarily driven by the large observed displacements to the south of the Denali/Totschunda junction (143.0–143.5°W in Figure 10e). It is interesting to note that the shallow components of the eastern patches abut a region of high coseismic slip. The close proximity of high coseismic slip and inferred shallow afterslip suggests that the inferred shallow afterslip could be a response to coseismically induced stresses.

6.5 Stress-Driven Afterslip

The upper mantle flow model that fits the observed far-field displacements well represents broadly distributed deformation within a viscoelastic medium. This is in contrast to the localized deformation along a deep continuation of the Denali fault in an otherwise elastic earth, represented by the afterslip model derived from inverting the GPS data. These two models can be seen as end-members of lithospheric rheology and deformation, both of which appear to provide a reasonable explanation to observed far-field displacements. However, as the inversion is not controlled by constitutive relations or coseismic loading of the fault, it is unclear whether the afterslip from the GPS inversion model represents a reasonable response to coseismic stress changes. In order to explore this question, we developed models in which frictionless slip can occur on a down-dip extension of the Denali fault in response to coseismic stress changes. By modeling frictionless slip these models represent the maximum afterslip we would expect

from coseismic stress changes, assuming that afterslip is not modified by a preexisting stress field. As it is beyond the capability of the finite element formulations we are using to simultaneously enforce coseismic slip and allow free slip in the same patch of fault, we restrict this study to slip below the seismogenic zone, primarily concentrating on the plausibility of deep afterslip models to explain observed far-field displacements.

We considered a series of models in which a down-dip extension of the Denali fault can slip postseismically below some locking depth through to the base of the model. These stress-driven afterslip models represent the maximum deep slip that can be driven by coseismic stress changes. We found a minimum misfit of 32 mm for a model of stress driven afterslip below a locking depth of 40 km. This is comparable to the misfit of the best-fitting viscoelastic models. Shallower locking depths led to higher misfits, as stress-driven afterslip in the 24 (minimum depth before intersecting the seismogenic zone) to 40 km depth range induced near-field surface displacements with significant azimuth errors. This does not exclude slip in this region, but suggests that such slip would be less than that calculated for a frictionless fault responding to coseismic stresses in this depth range. This is in contrast to stress-driven afterslip models with locking depths below 40 km. In such models the magnitude of calculated surface displacement decreased in both the near- and far-field well below observed values as the reservoir of coseismic stresses below 40 km was no longer being fully allowed to dissipate. This suggests that at least some mechanism of stress dissipation was active in the lower crust. We do not, however, place much significance on the 40 km depth limit, given that the stress-driven afterslip model alone is a very poor fit to the data. In the next section we consider multiple mechanism models in which the far-field deformation is explained mostly by viscoelastic relaxation of the mantle; in the multiple-mechanism models the inclusion of afterslip improves the fit to the data and the afterslip distribution may be physically realistic.

The calculated displacements due to the stress driven afterslip model (with a locking depth of 40 km) are compared to observed displacements in Figure 10f. The stress driven afterslip model can reasonably match far-field displacements to the south, but greatly underpredicts displacements at far-field stations to the north, and most of the near-field

sites. The far-field rms value of this model is 16 mm compared to 7 mm for the mantle flow model and 6 mm for the optimized afterslip inversion. Shallower afterslip (i.e. above 40 km depth) does not contribute significantly to far-field displacements. Numerical experimentation with straight faults leads us to believe that the asymmetry associated with stress driven afterslip arises from the curvature of the Denali fault, which focuses deformation to the south. This effect is muted in the viscoelastic mantle and crustal flow model, as relaxation occurs throughout a broad region as opposed to being confined along a sharp, curved fault.

Figure 14 shows the slip distribution that arises from frictionless stress-driven afterslip below a locking depth of 40 km. Stress-driven afterslip is broad, distributed along the full coseismic rupture length, with highest slip occurring directly beneath the region containing the highest coseismic slip patches. Afterslip in the stress driven model does not exceed 0.4 m, in contrast to the afterslip distribution inferred in the GPS inversion (Figure 13a). At a depth of 80 to 100 km, the inversion model finds afterslip of greater than 1 m compared to only 0.2 to 0.3 m for the stress driven model. Recall that the stress-driven afterslip model is frictionless, thus representing the maximum slip that should be expected to result from coseismic stresses. The GPS inversion model leads to 3 to 4 times the magnitude of afterslip that occurs in the stress driven model. Coseismic stress changes simply cannot drive the magnitude of afterslip inferred from the GPS inversion.

In the GPS inversion model deep afterslip is confined to a ~100-km-long section of the fault, roughly one third of the rupture length, and this region is shifted to the west with respect to the high coseismic slip patches. The more focused distribution of deep slip in the GPS inversion model likely results from the inversion working to minimize the asymmetric influence of fault curvature by focusing the slip on a smaller region. This in turn requires higher slip in order to match the far-field displacements. Explaining this distribution of afterslip would require implausible temporal and spatial variations in fault strength. The stress-driven afterslip model cannot explain the observed deformation by itself, as it cannot simultaneously explain far-field displacements to the north and south,

underpredicting the latter. From the standpoint of pure simplicity (Occam's razor), we conclude that broad flow in the upper mantle due to viscoelastic relaxation is the most plausible explanation for observed far-field displacements following the Denali earthquake.

6.6 Multiple Mechanism Models

A robust conclusion from our study of poroelastic rebound, viscoelastic relaxation, and afterslip, is that no single mechanism satisfactorily explains observations of postseismic surface deformation following the Denali earthquake. This is in contrast to Pollitz [2005], who suggests that postseismic deformation following the Denali earthquake can be explained solely by viscoelastic relaxation primarily in the upper mantle. We suggest that multiple postseismic mechanisms are in operation, which should not be surprising since each of the mechanisms considered has a solid physical basis for occurring. Following the previous arguments, we consider flow within a viscoelastic mantle (below 60 km) to be the best explanation for observed far-field displacements, and thus include it in all combination models. In addition, because we have no reason to assume that there are no crustal fluids or that permeabilities are too low for poroelastic rebound to occur, we also include the contribution of poroelastic flow in all combined models. We do not know the timescale required for complete poroelastic relaxation, but as previously discussed, other studies [Peltzer et al., 1996, 1998; Masterlark and Wang, 2002; Jónsson et al., 2003] suggest that the process should occur rapidly compared to the 2-year duration of this study. We calculate the contributions of mantle viscoelastic flow, poroelastic rebound, and interseismic block rotation to surface displacements and subtract this from the observed displacements, finding a residual set of displacements, which we attempt to match using additional mechanisms. This process is repeated for a range of upper mantle viscosities.

We initially consider that the residual displacements may be due to shallow afterslip and solve for the afterslip distribution by inverting the residual displacements. The inferred afterslip from this inversion is shown in Figure 13b (hereafter referred to as residual afterslip). Surface displacements from this model, combined with those due to

mantle flow and poroelastic rebound give an overall rms misfit of 17 mm based on all the data. This is about half the rms misfit of the best single mechanism models, and given the number of data, this reduction in misfit is highly significant (the optimized afterslip-only model has a comparable misfit but produces an implausible afterslip distribution, as discussed above). The residual afterslip model is comprised of three shallow patches as shown in Figure 13b, which also shows the contours of the high coseismic slip patches for comparison. The residual afterslip distribution is quite different at shallow depths from the calculated frictionless stress-driven afterslip distribution. It consists mainly of several discrete patches rather than a smooth distribution of afterslip.

The westernmost residual afterslip patch (centered at a depth of 36 km and an E-W distance of 80 km in Figure 13b) ranges from near the surface to well within the lower crust, and lies adjacent to and below a zone of high coseismic slip. This patch is instrumental in correcting azimuth and magnitude mismatches in the mantle flow model near the middle of the Denali fault (at longitude ~146°W in Figure 10d). The middle patch in the residual afterslip model (at a E-W distance of 180 km in Figure 13b), is primarily confined to the seismogenic upper crust and occurs adjacent to the patch of highest coseismic slip. Residual afterslip on the Totschunda fault has a shallow NW component that abuts a zone of large coseismic slip. However, the eastern part of this patch, which reaches all the way to the edge of the inversion model, lies within the lower crust beneath a part of the fault that had little coseismic slip. These easternmost patches, which also appeared in the full afterslip model (Figure 13a), are instrumental in greatly reducing displacement errors near the Denali/Totschunda junction. As previously noted, the close proximity of high coseismic slip and inferred shallow afterslip suggests that the inferred shallow afterslip could be a response to coseismically induced stresses. It is not clear why large afterslip would be found in the lower crust at the eastern edge of the inversion model, but it is difficult to explain the large postseismic displacements in this region without this afterslip.

Though we have previously excluded lower crustal flow as the primary source of postseismic displacements, we cannot rule out a contribution of lower crustal flow to a

multiple-mechanism model. We note that deeper lower crustal flow (Figure 10c) and upper mantle flow (Figure 10d) do not induce completely distinct surface displacements. Thus, there is some trade-off between viscoelastic flow in these two depth intervals. We explored this trade-off by taking the best-fitting rheologies from the single mechanism studies (insets of Figures 10c and 10d), and varying the average viscosity of each to find which combination leads to the minimum misfit in a multiple mechanism model that also includes residual afterslip, poroelastic rebound, and interseismic block rotation. The rms misfits from this set of models are shown in Figure 15a. The best-fitting model has an rms misfit of 12 mm, the smallest misfit of any model considered in this study (including the afterslip inversion). This model uses a mantle that is about one third the viscosity of the lower crust in their respective weakest regions; 3×10^{18} Pa s in the upper mantle compared to 1×10^{19} Pa s in the lower crust. An excellent fit between observed horizontal displacements and those calculated from this multiple mechanism model is shown in Figure 16a. The components and rheology of this model are shown in Figure 16b.

We finally considered the possibility that stress-driven afterslip within the lower crust and mantle lid may contribute to the postseismic displacements. Such a mechanism might be expected if the lower crust were relatively strong compared to a narrow shear zone. We thus considered a multiple-mechanism postseismic model that includes a viscoelastic mantle, residual afterslip, poroelastic rebound, interseismic block rotation, and coseismic-stress induced afterslip on a frictionless, down-dip continuation of the Denali fault. We considered models in which the locking depth ranged from 24 km (the base of the seismogenic zone) to 40 km depth, with slip allowed to occur to a depth of 60 km depth (just above where the mantle is inferred to readily flow). For mantle rheology, we again use the best-fitting viscosity profile from the single mechanism study (Figure 10d inset), and allow the average viscosity to vary. Figure 15b shows the rms misfits of these series of models as a function of locking depth and mantle viscosity. The best fitting model has stress driven afterslip below a depth of 30 km and a mantle viscosity at 120 km depth of 4×10^{18} Pa s, and has an rms misfit of 12 mm. This is a similar misfit to the multiple mechanism model that included lower crustal flow. Because the model already includes the residual afterslip distribution, which consists mostly of afterslip at

depths less than 30 km, models that also include stress-driven afterslip at shallower depths do not improve the fit to the data. The calculated horizontal displacements from this model (Figure 16c) are very similar to those of the multiple mechanism model that considers lower crustal flow. The components and rheology of this model are shown in Figure 16d.

These results suggest that either lower crustal flow or afterslip on the Denali fault within the lower crust, in conjunction with mantle flow, residual afterslip, poroelastic rebound, and secular block rotation, work well to explain the first two years of horizontal postseismic surface deformation. Future examination of the temporal evolution of the postseismic deformation may allow us to distinguish between these models. The difference in mantle rheology between the two models is minor, 3×10^{18} Pa s versus 4×10^{18} Pa s at 120 km depth. In deference to the seismic velocity models that suggest that the Denali fault may cut through to a depth of 60-65 km, we prefer the multiple mechanism model that includes afterslip on a down-dip extension of the Denali fault through the entire crust and thin mantle lid.

7.0 Vertical Displacement Constraints

As discussed previously, we did not consider vertical displacement constraints in our formal search of model space. Here we take the best-fitting models derived with the horizontal GPS constraints, calculate vertical displacements, and compare them to the observed vertical displacements from the continuous GPS stations as shown in Figure 17. Several observations can be made from these comparisons. With the only significant observed vertical displacements occurring near the Denali/Totschunda junction, and being almost exclusively uplift, none of the models considered in our analysis shows a good correspondence. With this situation, a quantitative assessment of the goodness of fit (rms) did not illuminate a best model. It is interesting to note that poroelastic rebound is the only mechanism calculated to generate vertical displacement primarily near the Denali/Totschunda junction (though this model predicts subsidence on the north side of the fault where observations suggest uplift). This is consistent with observations following the 1992 Landers quake, where the largest poroelastic effect was observed

around fault step-overs [Peltzer et al., 1996]. However, poroelastic rebound does not generate, and thus does not explain, significant observed horizontal surface displacements following the Denali earthquake.

It is unfortunate that more reliable vertical constraints are not yet available, especially since most of the continuous GPS stations fall outside of the regions where most of the models predict significant vertical displacements. Furthermore, even without considering horizontal constraints, we could find no combination of mechanisms that would explain uplift on both sides of the Denali/Totschunda junction and a general lack of vertical motions elsewhere. A longer time series of data and careful modeling of the seasonal signals will be necessary to make full use of the vertical data. It may be possible to extract a more precise and detailed picture of vertical deformation by integrating InSAR range-change measurements, however the steep topographic terrain, vegetation, snow and ice cover, and active atmosphere make this a difficult undertaking.

8.0 Conclusions and Inferences

We have developed a set of finite element models, constrained by GPS observations of surface deformation following the 2002 Denali earthquake to understand what processes govern postseismic deformation and to gain insights into the mechanical structure of the Alaskan lithosphere. Our preferred model is comprised of upper mantle flow, localized afterslip within the upper crust, poroelastic rebound, and afterslip on a down-dip extension of the Denali fault from ~30 to ~60 km depth. Afterslip within the lower crust is preferred over broad viscoelastic flow in the lower crust owing to the existence of seismic velocity discontinuities across the fault at depth, though our modeling does not favor either mechanism. Despite the excellent fit of our multiple mechanism model to observed horizontal GPS displacements, neither this, nor any of our other models are able to match inferred vertical tectonic displacements.

We find that no single mechanism: afterslip, viscoelastic flow, or poroelastic rebound, can explain the postseismic observations. Instead, a combination of contributing processes is required. This is in contrast to Pollitz [2005], who suggests that postseismic

deformation following the Denali earthquake can be explained solely by viscoelastic relaxation primarily in the upper mantle. However, the model of Pollitz [2005] leads to misfits to the data during the early part of the post-seismic period, which Pollitz attributes to common-mode noise. We find that these misfits are in fact the component of the data that require multiple mechanisms. A comparison of our models to that of Pollitz suggests that a large fraction of the afterslip we infer may have occurred within the first several months after the earthquake, which would be expected if the characteristic decay time for the afterslip is of the order of a few weeks to a couple of months.

A model of pure afterslip derived from GPS inversions can also explain the observed surface displacements, but consideration of stress-driven afterslip suggests that coseismic stress changes cannot induce the magnitude of deep afterslip obtained in the inversion model. Furthermore, the distribution of deep afterslip in the inversion model is concentrated in a relatively narrow region compared to the extent of the Denali rupture. This is in contrast to the inferred shallow slip patches in the GPS inversions, which, for the most part, appear to be adjacent to regions of large coseismic slip suggesting a causative relationship.

Though our results only span a relatively short 2-year postseismic period, where transient deformation may not be indicative of longer term processes, it is interesting to note that our inferences of the mechanical properties of the Alaska lithosphere are similar to that of other subduction zone backarc regions where properties are based on much longer duration observations. Namely, subduction zone backarcs tend to be characterized by having relatively thin lithospheres with thicknesses of the order of 50 to 60 km over considerable widths (100s of km), overlaying a weak asthenosphere [e.g., Hyndman et al., 2005]. The inferred effective viscosity of the mantle in our 2-yr study is almost identical to the 3×10^{18} Pa s value suggested by a 3-yr study by Pollitz et al. [2000] following the 1992 Landers quake, as is the 3:1 lower crust to mantle viscosity ratio, despite a significant difference in crustal thickness. The relatively low inferred viscosity of the mantle in these regions, compared to longer term global averages of $\sim 10^{20} - 10^{21}$ Pa s [e.g., Mitrovica and Forte, 1997; Peltier, 1998; Kaufmann and Lambeck, 2002;

Dixon et al., 2004], may be due to the short time span of the postseismic observations considered in combination with a stress-dependent rheology [e.g., Karato, 1993], where initially high coseismic stresses lead to initially low effective viscosities [e.g., Freed and Bürgmann, 2004; Pollitz, 2003]. These regions may have weaker rheologic strength due to high water concentration [e.g. Hirth and Kohlstedt, 2004], which may be due to hydration from subduction below and/or high heat flow [e.g. Humphreys et al., 2003; Dixon et al., 2004]. Finally, our inferred weaker upper mantle compared to the lower crust in our 2-yr study is in agreement with a variety of short and longer term studies that suggest that the traditional jelly sandwich profile of lithospheric strength (with a weak lower crustal layer and a strong lithospheric mantle) may be a rare occurrence [e.g. Pollitz et al, 2000; Jackson, 2002].

Acknowledgments:

The CGPS stations were installed by UNAVCO. We thank the UNAVCO engineers J. Sklar, B. Johns, J. Greenberg, and S. Borenstein for their efforts in the field, and Max Kaufman (UAF) for assisting with the later site installations and for tireless efforts to download data even in the depths of winter. We thank the Pacific Geoscience Center in Canada for sharing data from the BEA2 CGPS station. We are grateful to Donna Eberhart-Phillips for sharing with us the elastic structure of the Alaskan lithosphere derived from seismic velocities. Reviews by Jim Savage, Hilary Fletcher, and an anonymous associate editor, substantially improved the paper. This project is funded by NSF EAR grants 0309620-EAR and SGER-0312427-EAR to Purdue, EAR-0310410 and EAR-0328043 to UAF, and EAR-0309946 to UCB.

References

Altamimi, Z., P. Sillard, and C. Boucher, ITRF2000: A new release of the International Terrestrial Reference Frame for earth science applications, *J. Geophys. Res*., 10.1029/2001JB000561, 2002.

Bills, B. G., D. R. Currey, G. A. Marshall, Viscosity estimates for the crust and upper mantle from patterns of lacustrine shoreline deformation in the eastern Great Basin, *J. Geophys. Res., 99*, 22059-22096, 1994.

Booker, J. R., Time-dependent strain following faulting of a porous-medium, J. Geophys. Res., 79, 2037-2044, 1974.

Bosl, W. J. and A. Nur, Aftershocks and pore fluid diffusion following the 1992 Landers earthquake, J. Geophys. Res., 107, 2001JB000155, 2002.

Brocher, T. M., G. S. Fuis, W. J. Lutter, N. I. Christensen, and N. A. Ratchkovski, Seismic velocity models for the Denali Fault Zone along the Richardson Highway, Alaska, *Bull. Seismo. Soc. Am., 94*, S85-S106, 2004.

Buckman, R. C., G. Plafker, and R. V. Sharp, Fault movement (afterslip) following the Guatemala earthquake of February 4, 1976, Geology, 6, 170-173, 1978.

Bürgmann, R., S. Ergintav, P. Segall, E. H. Harding, S. C. McClusky, R. E. Reilinger, H. Woith, and J. Zschau, Time-dependent distributed afterslip on and deep below the Izmit earthquake rupture, *Bull. Seismo. Soc. Am., 92*, 126-137, 2002.

Calais, E., C. DeMets, and J.M. Nocquet, Evidence for a post-3.16 Ma change in Nubia-Eurasia plate motion, *Earth Planet. Sci. Let, 216*, 81-92, doi:10.1016/S0012-821X(03)00482-5, 2003.

Casarotti, E. and A. Piersanti, Postseismic stress diffusion in Chile and South Peru, *Earth Planet. Sci. Lett., 206*, 325-333, 2003.

Chéry, J, S. Carretier, and J. F. Ritz, Postseismic stress transfer explains time clustering of large earthquakes in Mongolia, *Earth Planet. Sci. Lett., 194*, 277-286, 2001.

DeMets C., R. G. Gordon, D. F. Argus, S. Stein, Effect of recent revisions to the geomagnetic reversal time-scale on estimates of current plate motions, Geophys. Res. Lett., 21, 2191-2194, 1994.

Deng, J., M. Gurnis, H. Kanamori, and E. Hauksson, Viscoelastic flow in the lower crust after the 1992 Landers, *Science, 282*, 1689-1692, 1998.

Dixon, J. E., T. H. Dixon, D. R. Bell, and R. Malservisi, Lateral variation in upper mantle viscosity: Role of water, *Earth Planet. Sci. Lett.*, *222*, 451-467, 2004.

Dreger, D. S., D. D. Oglesby, R. Harris, N. Ratchkovski, and R. Hansen, Kinematic and dynamic rupture models of the November 3, 2002 M_w7.9 Denali, Alaska, earthquake, Geophys. Res. Lett., 31, 2003GL018333, 2004.

Eberhart-Phillips, D., et al., The 2002 Denali fault earthquake, Alaska: A large magnitude, slip-partitioning event, *Science, 300*, 1113-1118, 2003a.

Eberhart-Phillips, D., D. H. Christensen, T. M. Brocher, U. Dutta, R. Hansen, and N. A. Ratchkovski, Imaging the transition from Aleutian subduction to Yakutat collision in central Alaska, with local earthquakes and active source data, Eos Trans. AGU, 84 Fall Mtg. Suppl., Abst. S21C-01, 2003b.

Fletcher, H. J., Crustal deformation in Alaska measured using the Global Positioning System, University of Alaska Fairbanks, 135pp., 2002.

Freed, A. M. and J. Lin, Delayed triggering of the 1999 Hector Mine earthquake by viscoelastic stress transfer, *Nature*, 411, 180-183, 2001.

Freed, A. M. and J. Lin, Accelerated stress buildup on the southern San Andreas Fault and surrounding regions caused by Mojave Desert earthquakes, *Geology*, 30*,* 571-574, 2002.

Freed, A. M. and J. Lin, Time-dependent changes in failure stresses following thrust earthquakes, *J. Geophys. Res., 103*, 24393-24409, 1998.

Freed, A. M. and R. Bürgmann, Evidence of power-law flow in the Mojave Desert mantle, *Nature, 430*, 548-551, 2004.

Freed, A. M., Earthquake triggering by static, dynamic, and postseismic stress transfer, *Annu. Rev. Earth Planet. Sci., 33*, 335-367, 2005.

Freymueller, J., S. Hreinsdóttir, C. Zweck, and P. Haeussler, The 1998-2002 Deep Megathrust Slip Event, Alaska, Eos Trans. AGU, 83(47), Fall Meet. Suppl., Abstract G61A-0972, 2002.

Hearn, E. H., R. Bürgmann, and R. E. Reilinger, Dynamics of Izmit earthquake postseismic deformation and loading of the Duzce earthquake hypocenter, *Bull. Seismol. Soc. Am., 92*, 172-193, 2002.

Hearn, E. H., What can GPS data tell us about the dynamics of post-seismic deformation?, Geophys. J. Int., 155, 753-777, 2003.

Hearn, E. H. and R. Bürgmann, The effect of elastic layering on inversions of GPS data for coseismic slip and resulting stress changes: Strike-slip earthquakes, *Bull. Seismol. Soc. Am.*, in press, 2005.

Heki, K., S. Miyazaki, and H. Tsuji, Silent fault slip following an interplate thrust earthquake at the Japan Trench, *Nature, 386*, 595-598, 1997.

Hirth, G., and D. L. Kohlstedt, Rheology of the upper mantle and the mantle wedge: a view from the experimentalists, in: J. Eiler (Ed.), Inside the Subduction Factory, *Am. Geophys. Union, Geophys. Monogr. Ser. 118*, 83-106, 2004.

Hreinsdottir S., J. T. Freymueller, R. Bürgmann, and J. Mitchell, Coseismic deformation of the 2002 Denali Fault Earthquake: Insights from GPS Measurements, *J. Geophys. Res., submitted*, 2005.

Hsu, Y. J., N. Bechor, P. Segall, S. B. Yu, L. C. Kuo, and K. F. Ma, Rapid afterslip following the 1999 Chi-chi, Taiwan earthquake, *Geophys. Res. Lett., 1029/2002GL014967*, 2002.

Hudnut, K. W., N. E. King, J. E. Galetzka, K. F. Stark, J. A. Behr, A. Aspiotes, S. van Wyk, R. Moffitt, S. Dockter, F. Wyatt, Continuous GPS observations of postseismic deformation following the 16 October 1999 Hector Mine, California, earthquake (M_w 7.1), *Bull. Seismol. Soc. Am.,* 92, 1403-1422, 2002.

Humphreys, E., E. Hessler, K. Dueker, G. Lang Farmer, E. Erslev, and T. Atwater, How Laramide-age hydration of North American lithosphere by the Farallon slab controlled subsequent activity in the western US, *Int. Geol. Rev., 45*, 575-595, 2003.

Hyndman, R. D., C. A. Currie, and S. P. Mazzotti, Subduction zone backarcs, mobile belts, and orogenic heat, *GSA Today*, *15*, 4-10, 2005.

Ivins, E. R., Transient creep of a composite lower crust .2. A polymineralic basis for rapidly evolving postseismic deformation modes, *J. Geophys. Res., 101*, 28005-28028, 1996.

Jacobs, A., D. T. Sandwell, Y. Fialko, and L. Sichoiz, The 1999 (M_w 7.1) Hector Mine, California, earthquake; near-field postseismic deformation from ERS interferometry, *Bull. Seismol. Soc. Am., 92*, 1470-1486, 2002.

Jackson, J., Strength of the continental lithosphere: Time to abandon the jelly sandwhich?, *GSA Today, 12*, 4-10, 2002.

Jónsson S., P. Segall, R. Pedersen, G. Björnsson, Post-earthquake ground movements correlated to pore-pressure transients, *Nature, 424*, 179-183, 2003.

Karato, S. and P. Wu, Rheology of the upper mantle: a synthesis, *Science, 260*, 771-778, 1993.

Kaufmann, G. and F. Amelung, Reservoir-induced deformation and continental rheology in the vicinity of Lake Mead, Nevada, *J. Geophys. Res., 105*, 16341-16358, 2000.

Kaufmann, G. and K. Lambeck, Glacial isostatic adjustment and the radial viscosity profile from inverse modeling, *J. Geophys. Res., 107*, 2001JB000941, 2002.

Kenner, S. J. and P. Segall, Lower crustal structure in northern California: Implications from strain rate variations following the 1906 San Francisco earthquake. *J. Geophys. Res., 108*, 10.1029/2001JB000189, 2003.

King, G. C. P. and M. Cocco, Fault interactions by elastic stress changes: new clues from earthquake sequences, *Adv. Geophys. 44*, 1-38, 2001.

King, R.W., and Y. Bock, Documentation for the GAMIT GPS software analysis, release 10.4, *unpublished*, 2004.

Kirby, S. H. and A. K. Kronenberg, Rheology of the lithosphere; selected topics. *Rev. Geophys. 25*, 1219-1244, 1987.

Lahr, J. C., and G. Plafker, Holocene Pacific-North American plate interaction in southern Alaska: Implications for the Yakataga seismic gap, *Geology*, 8, 483-486, 1980.

Marone, C. J., C. H. Scholz, R. Bilham, On the mechanics of earthquake afterslip, *J. Geophys. Res., 96*, 8441-8452, 1991.

Masterlark, T. and H. F. Wang, Transient stress-coupling between the 1992 Landers and 1999 Hector Mine, California, earthquakes, *Bull. Seismol. Soc. Am.,* 92, 1470-1486, 2002.

Mitrovica, J. X., and A. M. Forte, Radial profile of mantle viscosity: results from the joint inversion of convection and postglacial rebound observables, *J. Geophys. Res., 102*, 2751-2769, 1997.

Nostro, C, A. Piersanti, and M. Cocco, Normal fault interaction caused by coseismic and postseismic stress changes, *J. Geophys. Res., 106*, 19391-19410, 2001.

Nur, A. and J. R. Booker, Aftershocks caused by pore fluid-flow, *Science, 175*, 885-887, 1972.

Nur, A. and G. Mavko, Postseismic viscoelastic rebound, *Science, 183*, 204-206, 1974.

Oglesby, D. D., D. S. Dreger, R. A. Harris, N. Ratchkovski, and R. Hansen, Inverse kinematic and forward dynamic models of the 2002 Denali fault earthquake, Alaska, Bull. Seismo. Soc. Am., 94, S214-S233, 2004.

Ozacar, A. A., and S. L. Beck, The 2002 Denali Fault and 2001 Kunlun Fault earthquakes: complex rupture processes of two large strike-slip events, Bull., Seis. Soc. Amer., 94, S278-S292, 2004.

Peltier, W. R., Post-glacial variations in the level of the sea: implications for climate dynamics and solid earth geophysics, *Rev. Geophys., 36*, 603-689, 1998.

Peltzer G, P. Rosen, F. Rogez, and K. Hudnut, Postseismic rebound in fault step-overs caused by pore fluid flow, *Science, 273*, 1202-1204, 1996.

Peltzer G, P. Rosen, F. Rogez, and K. Hudnut, Poroelastic rebound along the Landers 1992 earthquake surface rupture, *J. Geophys. Res., 103*, 30131-30145, 1998.

Plafker, G., J. C. Moore, G. R. Winkler, Geology of the Southern Alaska Margin, in The Geology of Alaska, *Geol. Soc. Amer., Boulder, CO, G-1*, 389-449, 1994.

Pollitz, F. F. and S. I. Sacks, Consequences of stress changes following the 1891 Nobi earthquake, Japan, *Bull. Seismol. Soc. Am., 85*, 796-807, 1995.

Pollitz, F. F. and S. I. Sacks, The 1995 Kobe, Japan, earthquake; a long-delayed aftershock of the offshore 1944 Tonankai and 1946 Nankaido earthquakes, Bull. Seismol. Soc. Am., 87, 1-10, 1997.

Pollitz, F. F., R. Bürgmann, and B. Romanowicz B., Viscosity of oceanic asthenosphere inferred from remote triggering of earthquakes, *Science, 280*, 1245-1249, 1998a.

Pollitz F. F., R. Bürgmann, and P. Segall, Joint estimation of afterslip rate and postseismic relaxation following the 1989 Loma Prieta earthquake, J. Geophys. Res., 103, 26975-26992, 1998b.

Pollitz, F. F., G. Peltzer, and R. Bürgmann, Mobility of continental mantle; Evidence from postseismic geodetic observations following the 1992 Landers earthquake. *J. Geophys. Res., 105,* 8035-8054, 2000.

Pollitz, F. F., C. Wicks, and W. Thatcher, Mantle flow beneath a continental strike-slip fault; postseismic deformation after the 1999 Hector Mine earthquake, *Science, 293*, 1814-1818, 2001.

Pollitz, F. F. and S. I. Sacks, Stress triggering of the 1999 Hector Mine earthquake by transient deformation following the 1992 Landers earthquake, *Bull. Seismol. Soc. Am.* 92, 1487-1496, 2002.

Pollitz, F. F., Transient rheology of the upper mantle beneath central Alaska inferred from the crustal velocity field following the 2002 Denali earthquake, *in press J. Geophys. Res.,* 2005.

Ratchkovski, N. A., S. Wiemer, and R. A. Hansen, Seismotectonics of the central Denali fault, Alaska and the 2002 Denali fault earthquake sequence, *Bull. Seis. Soc. Amer.,* , 2005.

Reilinger, R.E., S. Ergintav, R. Bürgmann, S. McClusky, O. Lenk, A. Barka, O. Gurkan, L. Hearn, K.L. Feigl, R. Cakmak, B. Aktug, H. Ozener, and M.N. Töksoz (2000), Coseismic and postseismic fault slip for the 17 August 1999, M=7.5, Izmit, Turkey earthquake, *Science*, *289*, 1519-1524.

Rice, J. R. and M. P. Cleary, Some basic stress diffusion solutions for fluid-saturated elastic porous-media with compressible constituents, *Rev. Geophys., 14*, 227-241, 1976.

Richter, D. H. and N. A. Matson, Quaternary faulting in the eastern Alaska range, *Geol. Soc. Amer. Bull., 82*, 1529-1539, 1971.

Ridgway, K. D., J. M. Trop, W. J. Nokleberg, C. M. Davidson, K. R. Eastham, Mesozoic and Cenozoic tectonics of the eastern and central Alaska Range; progressive basin development and deformation in a suture zone, *Geol. Soc. Amer. Bull., 114*, 1480-1504, 2002.

Roeloffs, E., Poroelastic techniques in the study of earthquake-related hydrological phenomena, *Adv. Geophys., 37*, 135-195, 1996.

Sauber, J., S. McCluskey, and R. King, Relation of ongoing deformation rates to the

subduction zone process in southern Alaska, Geophys. Res. Lett., 24, 2853–2856, 1997.

Savage, J. C. and J. P. Church, Evidence for postearthquake slip in Fairview Peak, Dixie-Valley, and Rainbow Mountain Fault areas of Nevada, *Bull. Seis. Soc. Amer., 64*, 687-698, 1974.

Savage, J. C. and W. H. Prescott, Asthenosphere readjustment and the earthquake cycle, *J. Geophys. Res., 83*, 3369-3376, 1981.

Savage, J. C., Equivalent strike-slip earthquake cycles in half-space and lithosphere-asthenosphere earth models, *J. Geophys. Res., 95*, 4873-4879, 1990.

Savage, J. C. and J. L. Svarc, Postseismic deformation associated with the 1992 M-w=7.3 Landers earthquake, southern California, *J. Geophys. Res., 102*, 7565-7577, 1997.

Savage, Svarc, Prescott, JGR, 2003.

Segall, P., R. Bürgmann, and M. Mathews, Time-dependent triggered afterslip following the 1989 Loma Prieta earthquake, *J. Geophys. Res., 105*, 5615-5634, 2000.

Stein, R. S., The role of stress transfer in earthquake occurrence. *Nature, 402*, 605-609, 1999.

Stein, R. S., Earthquake conversations, *Sci. Amer., 288*, 72-79, 2003.

Stout, J. H. and C. G. Chase, Plate kinematics of the Denali fault system, *Can. J. Earth Sci*., 17, 1527-2537, 1980.

Thatcher, W., T. Matsuda, T. Kato, and J. B. Rundle, Lithospheric loading by the 1896 Riku-u earthquake, northern Japan; Implications for plate flexure and asthenospheric rheology. *J. Geophys. Res. 85*, 6429-6435, 1980.

Vergnolle, M., Pollitz, F., and E. Calais, Constraints on the viscosity of the continental crust and mantle from GPS measurements and postseismic deformation models in Western Mongolia, *J. Geophys. Res., Vol. 108, No. B10, 2502*, doi: 10.1029/2002JB002374, 2003.

Wright, T. J., Z. Lu, and C. Wicks, Constraining the slip distribution and fault geometry of the M_w7.9, 3 November 2002, Denali fault earthquake with interferometric synthetic aperture radar and global positioning system data, Bull. Seismo. Soc. Am., 94, S175-S189, 2004.

Zeng, Y., Viscoelastic stress-triggering of the 1999 Hector Mine earthquake by the 1992 Landers earthquake, *Geophys. Res. Lett., 28*, 3007-3010, 2001.

Zweck, C., J. T. Freymueller, and S. C. Cohen, Elastic dislocation modeling of the postseismic response to the 1964 Alaska Earthquake, *J. Geophys. Res.*, 2001JB000409, 2002.

Figure Captions

Figure 1. Topography and faulting in southern Alaska. The Pacific Plate subducts obliquely beneath North America at the Aleutian megathrust at a rate of 5.4 cm/yr [DeMets et al., 1994]. The Denali fault accommodates some of this in the form of shear strain within the North American plate. The dashed black/white lines denote the extent of the 2002 Denali earthquake rupture surface. Inset shows the larger regional setting. Continuous and campaign GPS stations used in this study are denoted with filled and unfilled triangles, respectively. Note that this GPS set utilized only stations above a latitude of 62°N, as displacements at stations to the south are influenced by subduction-related factors not considered in the models (see text).

Figure 2. Inference of tectonic displacement in (a) east, (b) north, and (c) vertical directions from continuous GPS time series (station MENT). Observed position time series (red lines) are modeled using equation 1 (see text) by solving for parameters associated with secular, logarithmic, annual, and semi-annual components (green lines). The tectonic model (secular and logarithmic terms only) are used to determine cumulative 2-year displacements for our postseismic analysis.

Figure 3. GPS observed total horizontal displacements from November, 2002 through November, 2004 with 95% confidence level error ellipses. Inset: observed vertical surface deformations from continuous GPS stations with 95% confidence level error bars.

Figure 4. Finite element mesh that incorporates the Denali rupture zone and regional block geometry. (a) Top view showing the correspondence of the mesh to southern Alaska. The cylindrical shape is driven by the need to incorporate motion of a cylindrical block bounded on the north by the Denali fault (see text). (b) Blow-up of the mesh within the box in (a) showing how the mesh incorporates the Denali rupture geometry (thick gray lines). (c) Isometric view showing model boundary conditions. The black and white dashed line indicates a lithospheric fault that cuts through the entire model to enable rotation of the inner cylindrical block. Velocity boundary conditions are applied

to generate a rotation of the inner block consistent with the inferred long-term slip rate of the Denali fault [Fletcher, 2002]. The lithospheric fault is locked to a depth of 15 km in the preseismic analysis, which generates an ~50-km-wide elastic strain accumulation zone across the Denali fault in general agreement with prequake observations [Figure 5, Fletcher, 2002]. The breadth and depth of the mesh is large enough such that coseismic stress changes induced by the Denali earthquake are not significant at the boundaries. Thus, the fixed components of the boundary conditions do not influence model results.

Figure 5. Pre-Denali earthquake GPS [Fletcher, 2002] and modeled velocities relative to station FAIR. Velocities at stations GNAA and TAZL are influenced by the subduction zone to the south and are not well predicted by this model. Southerly velocity component observed at station HURR is believed to be a result of continued postseismic deformation following the 1964 Alaska earthquake [Fletcher, 2002], which is not considered in our modeling.

Figure 6. Coseismic slip model of the 2002 Denali earthquake. The color coded portion is based on inversion of coseismic GPS data and observed surface offsets [Hreinsdottir et al., 2005]. Extended, uncolored contours represents deep slip added in the present analysis to compensate for the difference between a layered elastic structure (this analysis) and an elastic half-space (the GPS inversion). Center panel shows the earthquake rupture (red line) and fault model (green line) used in the inversion. The Denali fault (upper panel) is divided into seven planes (DF1-7), Totschunda fault (lower right panel) in two (TF1-2), and the Susitna Glacier fault (lower left panel) in two (SGF1-2). In addition to the estimated slip distribution (color contours), vectors indicating slip magnitude and direction are also shown (the arrows represent slip of the north face of the fault relative to the south face). Aftershocks are from Ratchkovski et al. [2005]. The hypocenter is indicated with red stars. TAP-Trans-Alaska pipeline. Faults from Plafker et al. [1994]. This figure was modified from an original figure of Hreinsdottir et al. [2005].

Figure 7. Elastic structure (shear modulus) as a function of depth in the region around and below the Denali fault derived from observed seismic velocities [Eberhart-Phillips, 2003b]. Black line shows the 2002 Denali rupture surface.

Figure 8. Average elastic strength as a function of depth in the Denali region based on the structure shown in Figure 7.

Figure 9. (a) Comparison of observed and calculated coseismic deformation associated with the 2002 Denali earthquake. Assumed coseismic slip is shown in Figure 6 (including deep slip to 24 km). (b) Subset of deformation field (box in a) showing how a shallower (only 18 km depth) slip model derived from a half-space inversion, but used in a layered earth forward model, underpredicts the GPS data.

Figure 10. Comparison of GPS observed and calculated horizontal surface displacement due to (a) 2 years of interseismic block rotation and various candidate postseismic mechanisms: (b) poroelastic rebound, (c) lower crustal flow, (d) upper mantle flow, (e) afterslip from GPS inversion, and (f) stress-driven afterslip in a down-dip extension of the Denali fault. Shown are total displacements for the two-year period from November, 2002 through November, 2004. The calculated displacements due to block rotation (a) have been subtracted from the observed postseismic displacements in these figures in order to more directly compare postseismic transients. For clarity we do not show the error ellipses for the observed data, these can be found in Figure 3. Each of these panels represents the best-fit model for the mechanism considered, with the parameter values shown in the insets. For the afterslip model from inversion (e), refer to Figure 13a for the slip distribution. For the stress driven afterslip model (f), refer to Figure 14.

Figure 11. Assumed rheologies and associated misfits for viscoelastic relaxation models. (a) Viscosity bounds of lower-crustal flow models considered. Red lines are models with uniform viscosity with depth. Green, blue, black, and cyan lines represent models in which viscosity varied by 1, 2, 3, and 4 orders of magnitude, respectively, within the depth region considered. For each viscosity profile, between 30 and 50 models with

varying base viscosities were run. Corresponding rms misfits for horizontal displacements calculated as a function of viscosity profile and base viscosity for lower-crustal flow models (b) for all GPS stations and (c) for 11 far-field (≥100 km from rupture surface) stations only. (d, e, f) Corresponding plots for upper mantle flow models.

Figure 12. Calculated (a) coseismic, (b) postseismic and (c) the difference (postseismic minus coseismic) shear stresses (planes parallel to fault surface) for the 2002 Denali earthquake based on a model of upper-mantle flow constrained by far-field surface deformations. Regions of stress decrease (blue in c) show where coseismic stresses relax postseismically in the mantle. Regions of stress increase (red in c) in the crust result from a transfer of stress from the relaxing mantle.

Figure 13. (a) Slip distribution for an afterslip model based on an inversion of horizontal GPS displacements from November 2002 through November 2004. (b) Slip distribution for an afterslip model based on the inversion of residual data after calculated surface displacements due to a mantle flow, poroelastic rebound, and interseismic block rotation were subtracted from the GPS observations. For comparison, 1 m, 5m and 9m contours of coseismic slip are superimposed on the afterslip distributions.

Figure 14. Calculated stress-driven afterslip on a frictionless, down-dip extension of the Denali fault from 40 km depth to the base of the model (240 km). Regions of coseismic slip in upper crust are shown for reference as to the extent of coseismic slip and the relative location of high-coseismic-slip patches.

Figure 15. Misfit of multiple-mechanism models that consider poroelastic rebound, shallow afterslip, viscoelastic flow in the mantle, interseismic block rotation, and (a) viscoelastic flow in the lower crust or (b) stress-driven afterslip of a down-dip extension of the Denali fault to a maximum depth of 60 km. In (a), misfit is calculated as a function of lower crust and upper-mantle viscosity profiles. In (b), misfit is calculated as

a function of mantle viscosity and the afterslip locking depth (the depth above which the fault is locked).

Figure 16. Comparison of GPS observed and calculated horizontal surface displacements for best-fitting multi-mechanism postseismic models. Models consider poroelastic rebound, shallow afterslip (Figure 14b), upper mantle flow, and (a) lower crustal flow or (b) stress-driven afterslip within the lower crust and mantle lid. Shown are total displacements for the two-year period from November, 2002 through November, 2004. Calculated displacements due to 2 years of interseismic block rotation (Figure 10a) have been subtracted from observed postseismic displacements in order to more directly compare postseismic transients.

Figure 17. Comparison of two years of GPS observed (bars) and model calculated (contours) vertical surface displacements due to various candidate postseismic mechanisms: (a) poroelastic rebound, (b) lower crustal flow, (c) upper mantle flow, (d) afterslip from GPS inversion, (e) multiple mechanism model including poroelastic rebound, shallow afterslip, lower crustal flow, and upper mantle flow, and (f) multiple mechanism model similar to (e), except that it considers slip on a down-dip extension of the Denali fault from 30 to 60 km instead of lower crustal flow.

Table 1. Total observed displacement from Nov., 2002 thru Nov., 2004 and associated one standard deviation formal errors (σ). Extraction of tectonic uplift from campaign GPS sites was not obtainable (see text).

Site	Longitude	Latitude	D_e (mm)	D_n (mm)	D_u (mm)	σ_e (mm)	σ_n (mm)	σ_u (mm)
Continuous Stations:								
CENA	-144.678	65.498	8.0	-18.9	-16.7	6.6	4.8	22.7
CLGO	-147.861	64.874	11.2	-27.0	-4.5	5.7	4.3	18.2
DNLC	-145.888	63.695	59.2	-48.0	-3.5	5.7	4.3	16.4
DRMC	-144.304	62.714	-103.0	150.2	38.0	7.6	4.3	17.2
FAIR	-147.499	64.978	17.2	-28.3	-9.0	4.3	4.5	14.0
FRIG	-143.005	62.411	-45.8	138.3	18.0	5.6	4.0	20.0
GNAA	-145.970	62.112	-40.5	43.9	3.0	5.9	9.5	24.0
HIWC	-148.807	63.464	-31.8	-5.7	0.0	4.9	7.2	17.0
HURC	-149.609	62.999	-37.6	-8.8	-1.0	5.2	3.8	16.0
JANL	-143.906	63.569	60.7	-26.0	5.0	5.3	5.1	16.0
LOGC	-143.345	63.023	72.2	26.6	28.0	22.2	8.6	28.0
MENT	-143.704	62.832	-67.3	149.4	68.0	6.6	4.5	17.0
PAXC	-145.452	62.969	-130.7	66.2	11.0	4.5	5.8	12.0
TLKA	-150.420	62.308	-30.5	-12.1	10.0	10.1	5.3	20.0
Campaign Stations:								
0999	-142.275	63.665	60.7	-8.4	N/A	10.0	4.0	N/A
ATT_	-145.847	63.502	81.0	-47.0	N/A	18.0	10.0	N/A
BRWN	-149.295	64.171	5.0	-17.0	N/A	9.0	6.0	N/A
BSB4	-145.789	63.907	63.2	-52.7	N/A	7.0	11.0	N/A
DNL1	-145.494	63.033	-137.8	74.2	N/A	15.6	12.9	N/A
DNL2	-145.854	63.516	73.6	-39.1	N/A	13.9	13.3	N/A
DNL3	-143.340	63.372	81.6	14.6	N/A	12.1	6.0	N/A
DFLY	-148.920	63.794	0.0	-16.5	N/A	7.0	7.0	N/A
DH34	-146.366	63.086	-92.2	42.9	N/A	12.0	12.0	N/A
DH97	-147.855	63.265	-79.2	5.3	N/A	10.0	4.0	N/A
DNLY	-145.888	63.695	70.8	-59.4	N/A	12.0	9.0	N/A
FCRK	-145.475	63.091	-138.3	67.4	N/A	10.0	9.0	N/A
GRIZ	-148.833	63.652	-10.1	-11.9	N/A	10.0	6.0	N/A
HIW4	-148.807	63.464	-36.0	-4.0	N/A	10.0	10.0	N/A
HURR	-149.609	62.999	-26.0	-16.1	N/A	9.0	6.0	N/A
L2C6	-148.866	63.383	-38.6	1.0	N/A	9.0	7.0	N/A
M110	-148.187	63.306	-69.6	-12.0	N/A	8.0	9.0	N/A
MEN_	-143.795	62.910	-50.6	119.3	N/A	9.0	6.0	N/A
NENA	-149.080	64.579	10.0	-24.7	N/A	12.0	6.0	N/A
PANA	-148.820	63.484	-31.3	-3.0	N/A	7.0	9.0	N/A
PISA	-149.211	63.285	-34.2	1.0	N/A	7.0	8.0	N/A
R109	-148.647	63.395	-49.1	-10.7	N/A	6.0	6.0	N/A
RBOW	-145.687	63.311	-74.7	5.0	N/A	10.0	10.0	N/A
ROLL	-143.297	62.536	-78.7	177.7	N/A	12.0	9.0	N/A
SSWB	-149.090	63.341	-23.7	-13.7	N/A	4.0	6.0	N/A
TAZL	-145.433	62.080	-20.0	64.7	N/A	9.0	4.0	N/A
TINA	-142.026	63.113	62.6	2.5	N/A	5.0	6.0	N/A

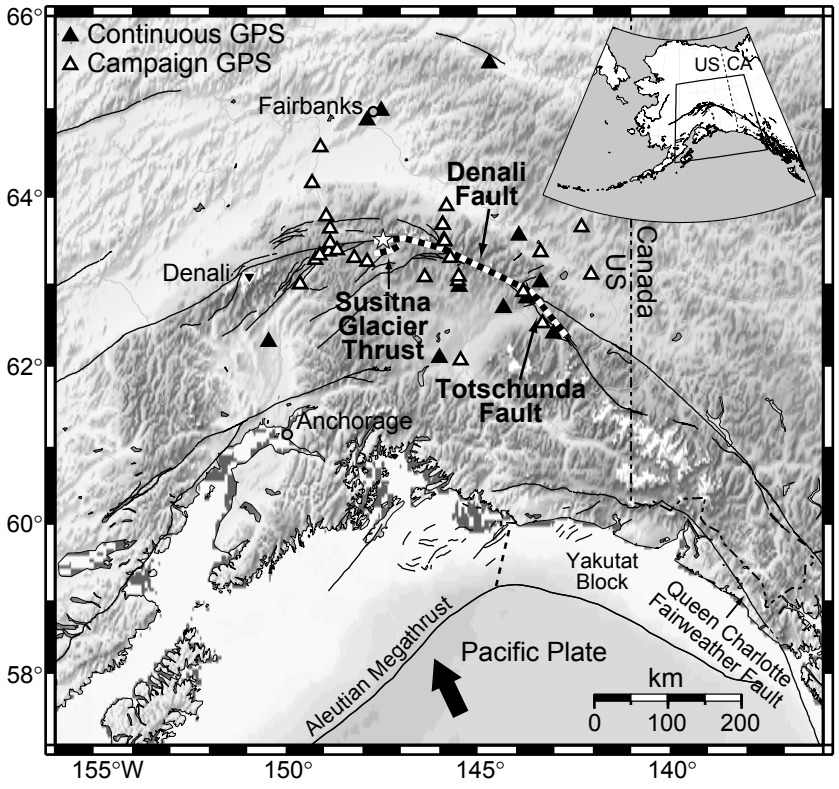

Freed et al., Figure 1

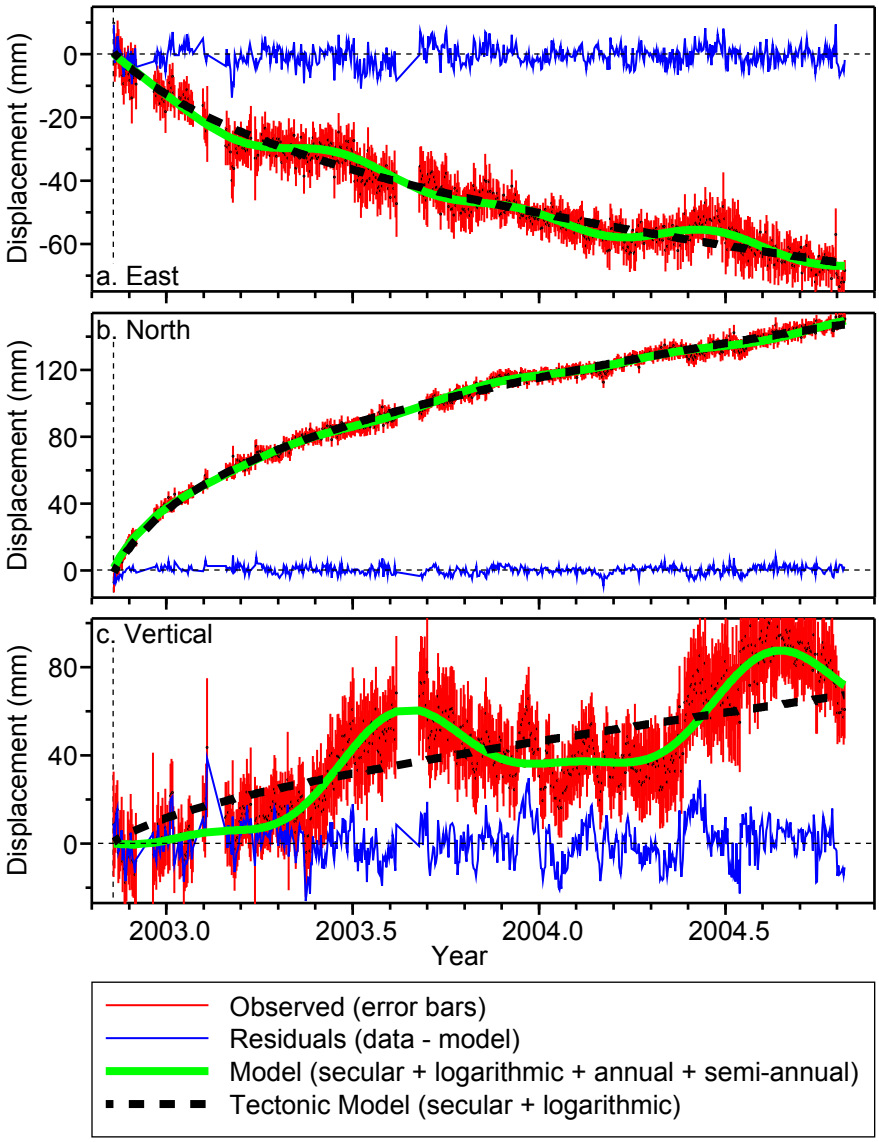

Freed et al., Figure 2

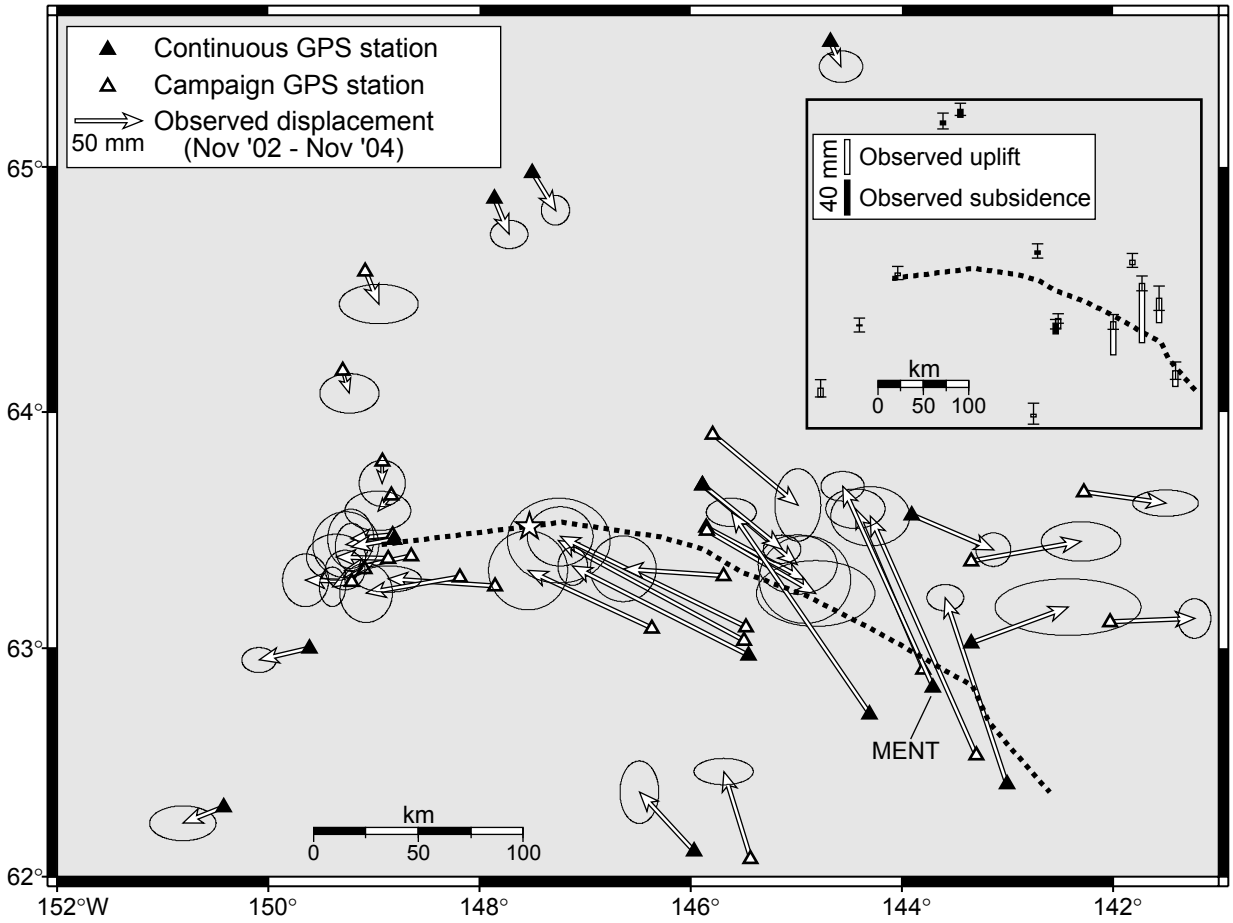

Freed et al., Figure 3

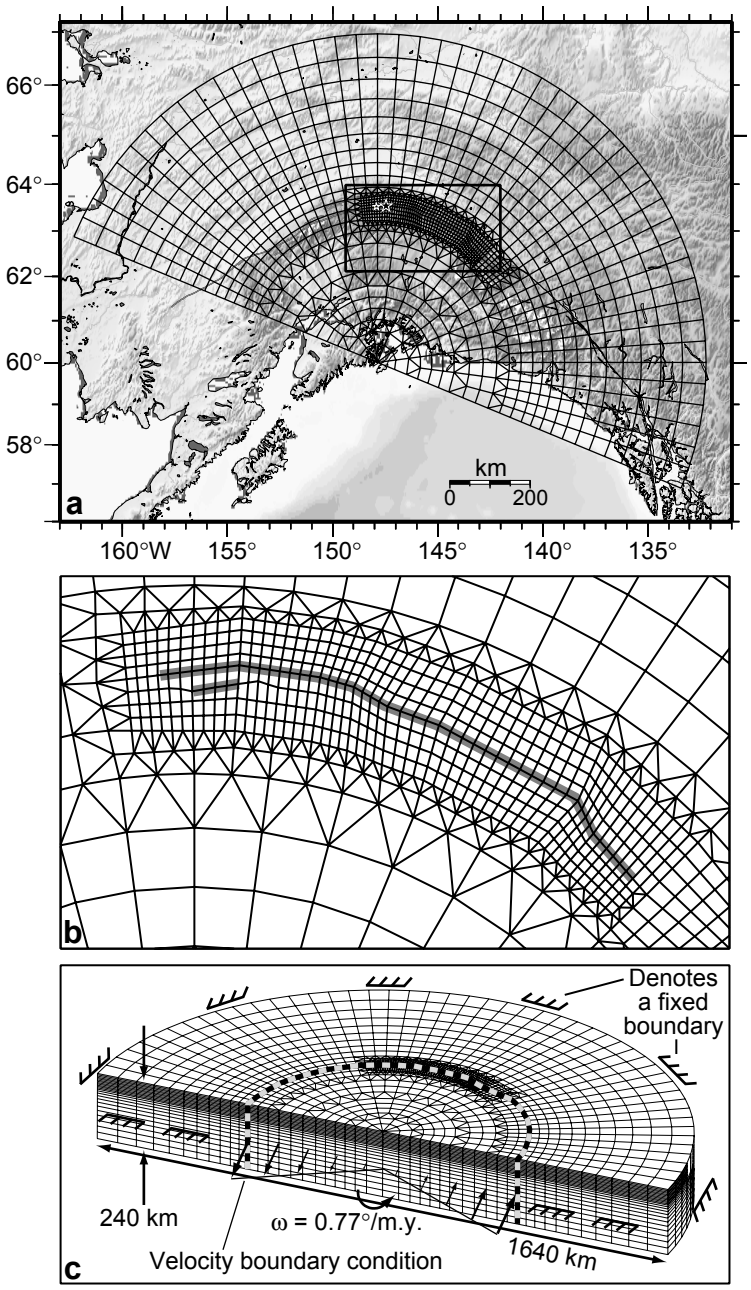

Freed et al., Figure 4

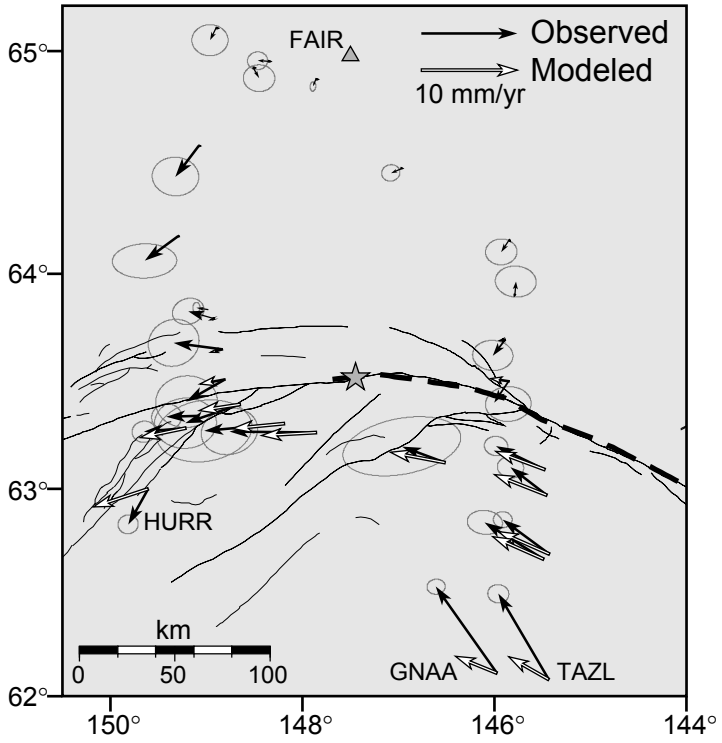

Freed et al., Figure 5

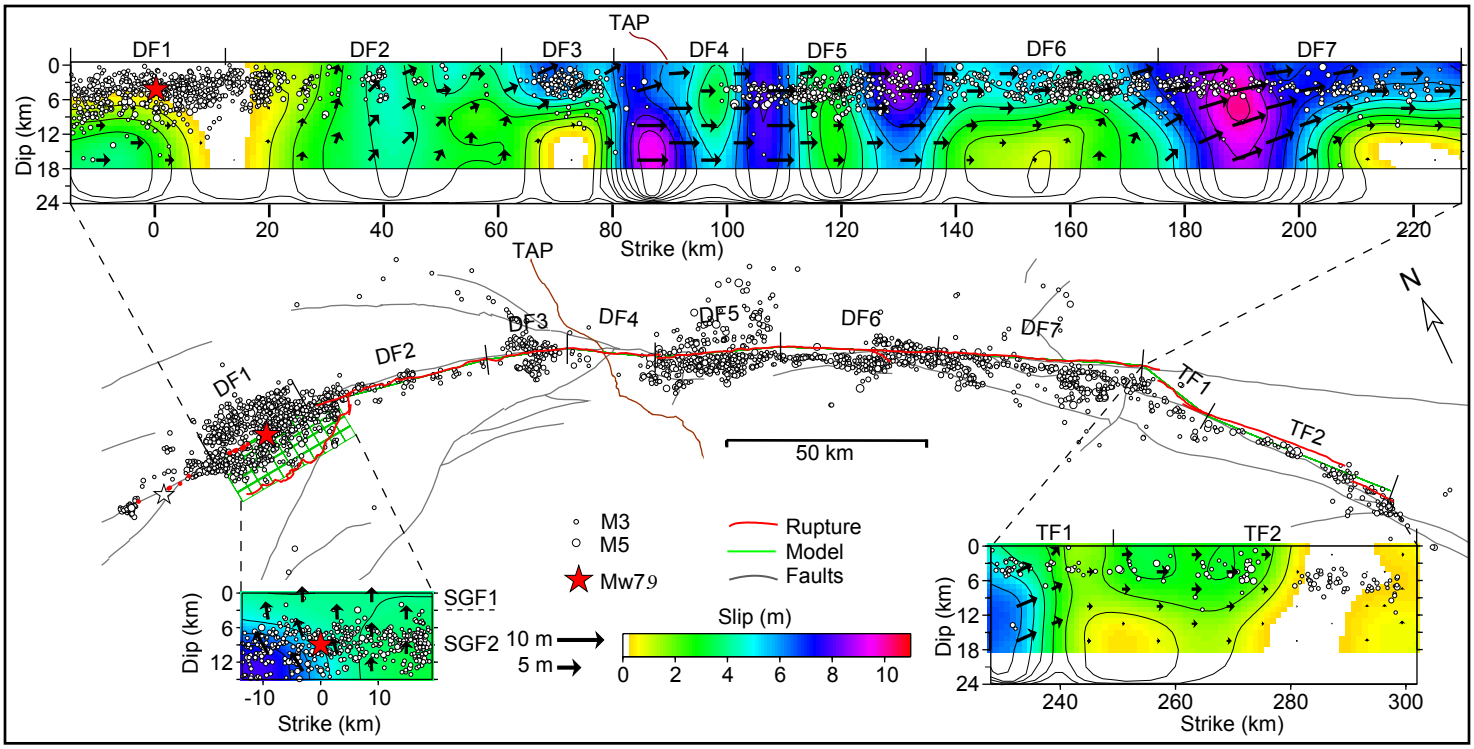

Freed et al., Figure 6

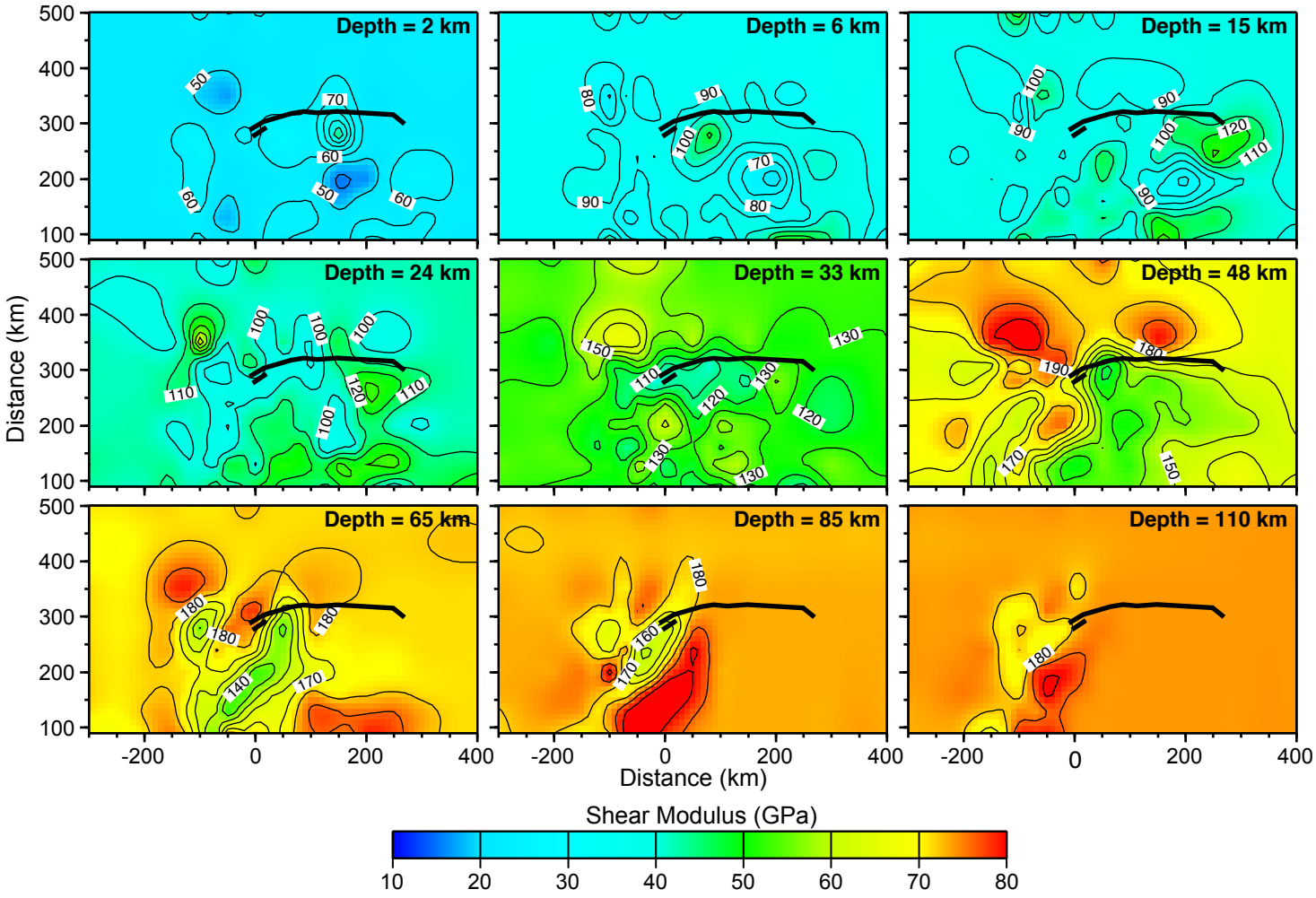

Freed et al., Figure 7

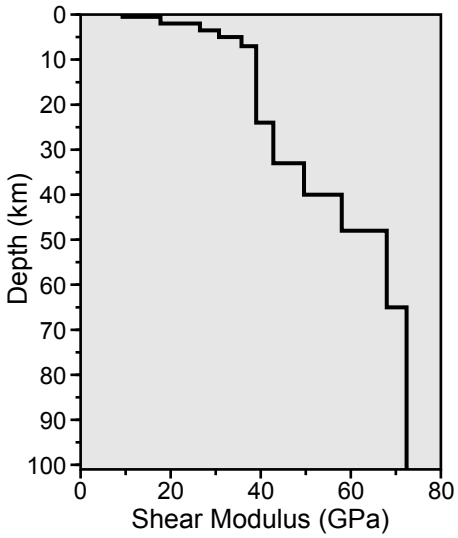

Freed et al., Figure 8

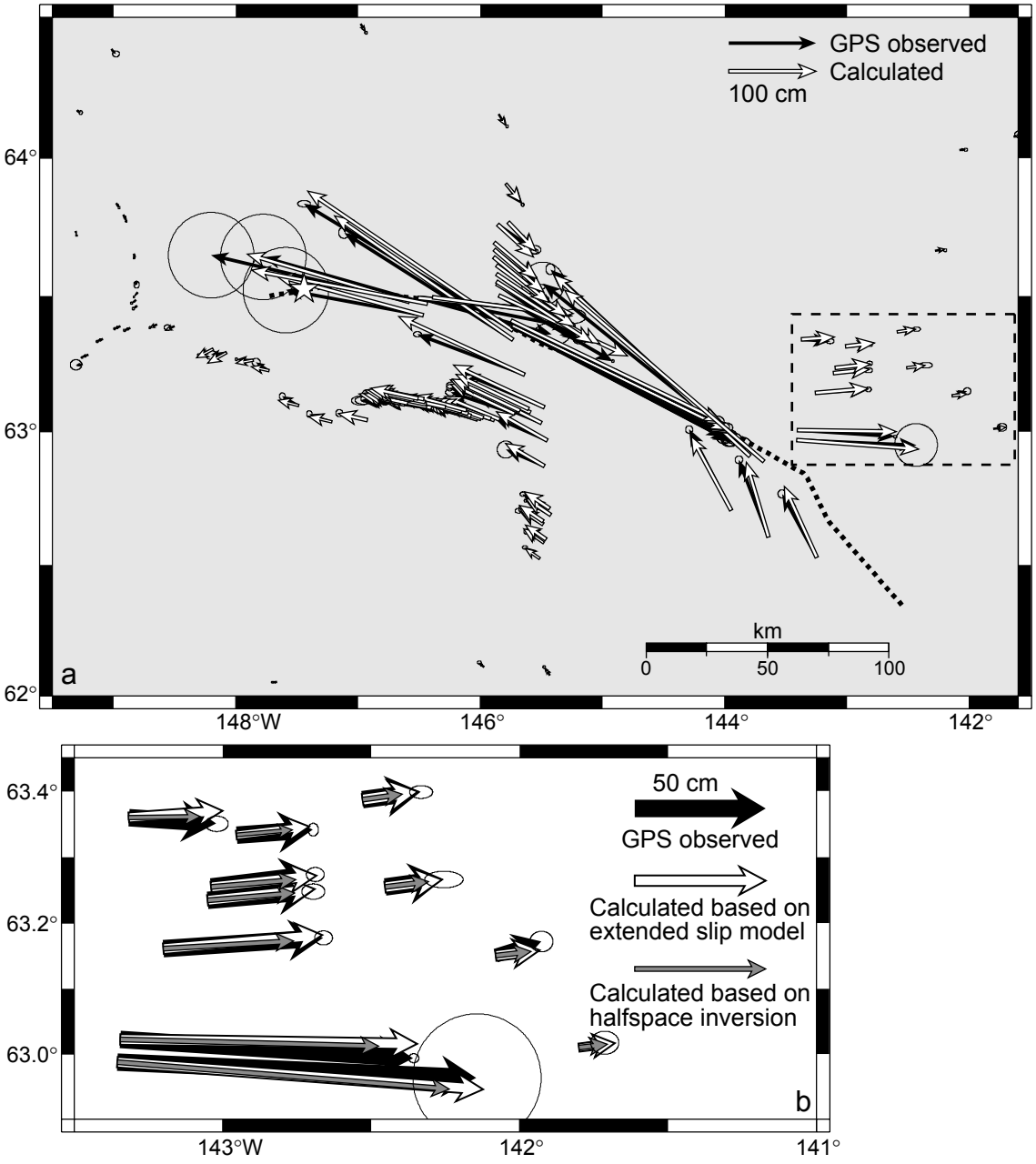

Freed et al., Figure 9

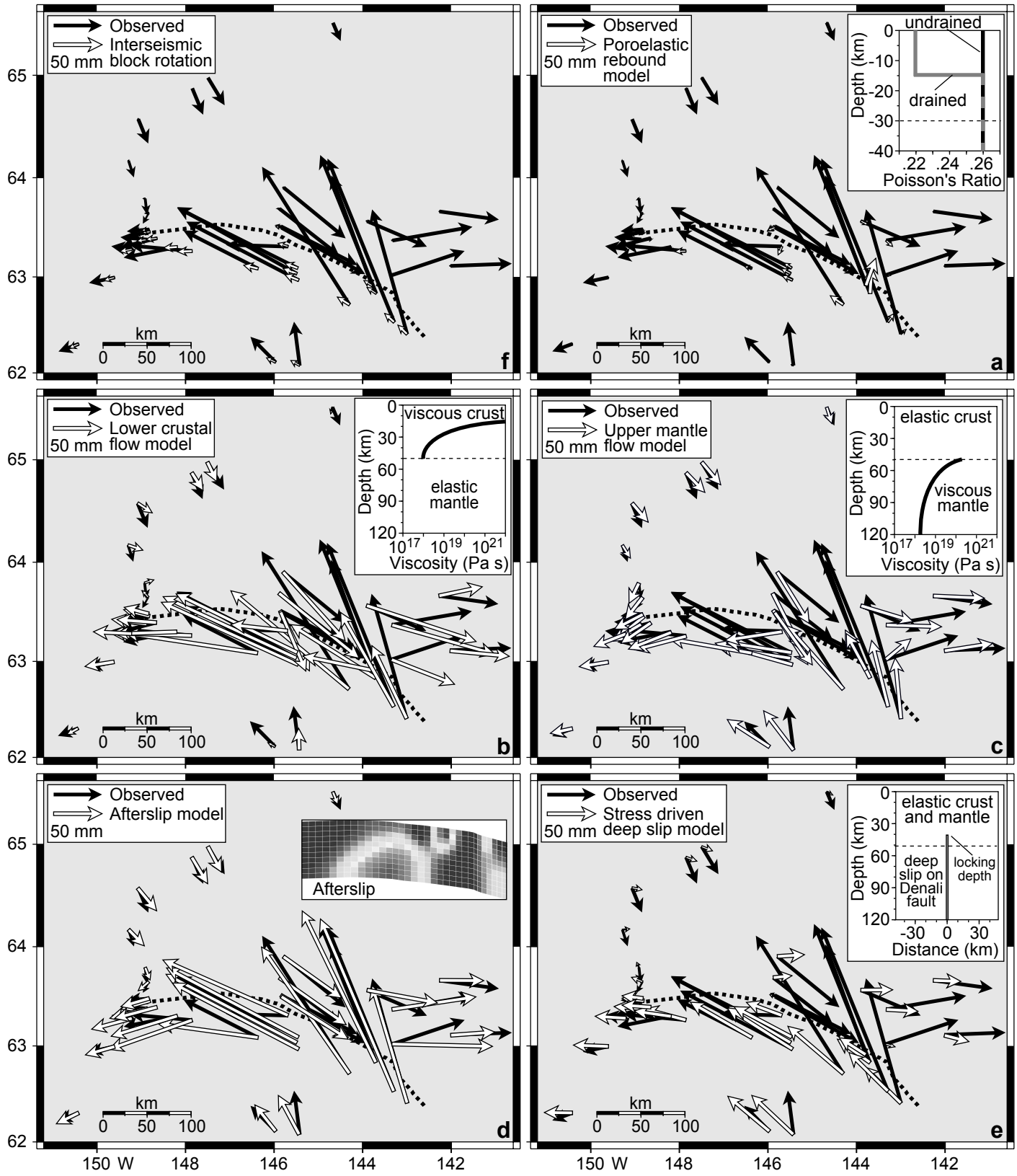

Freed et al. Figure 10

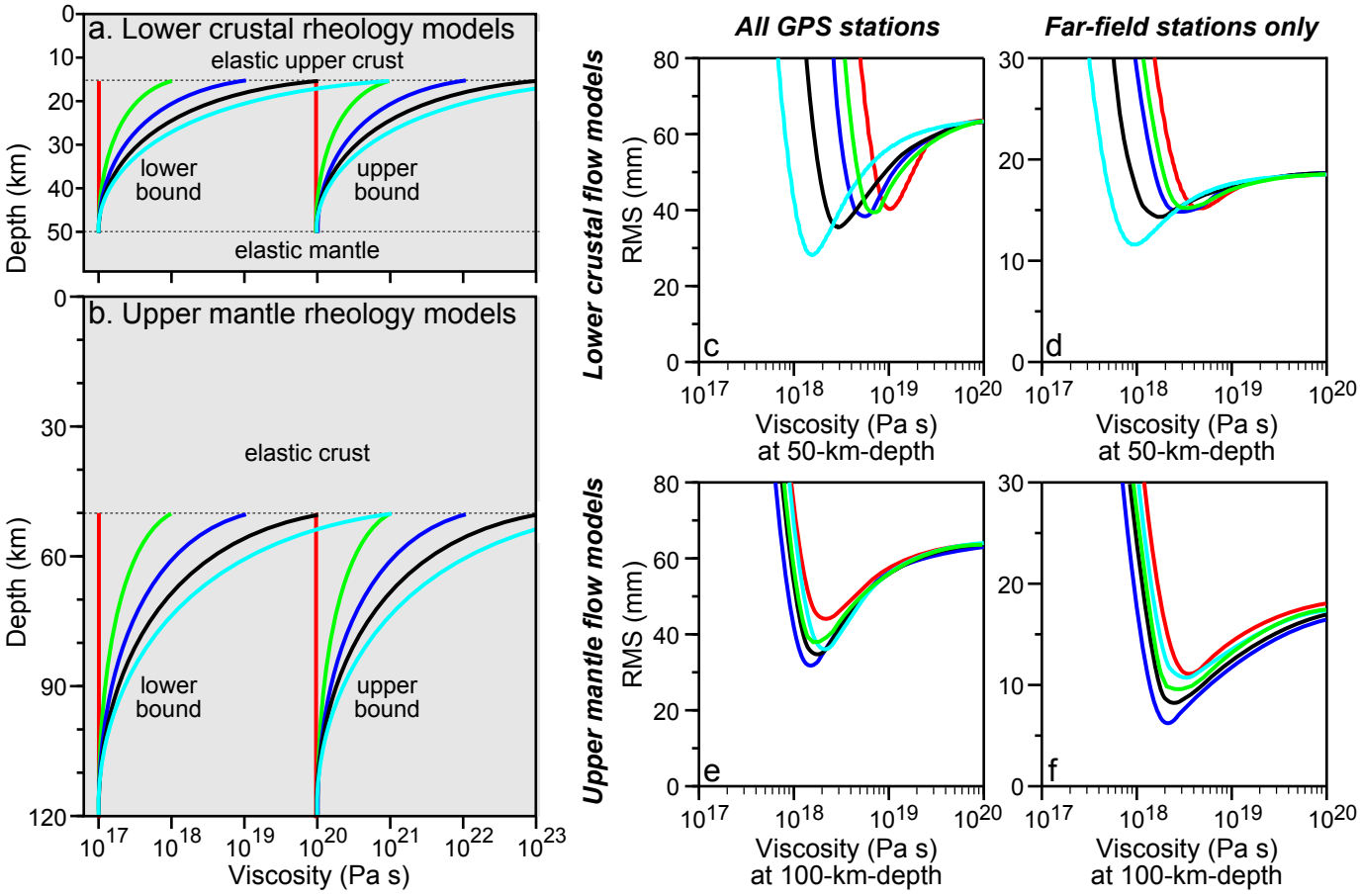

Freed et al. Figure 11

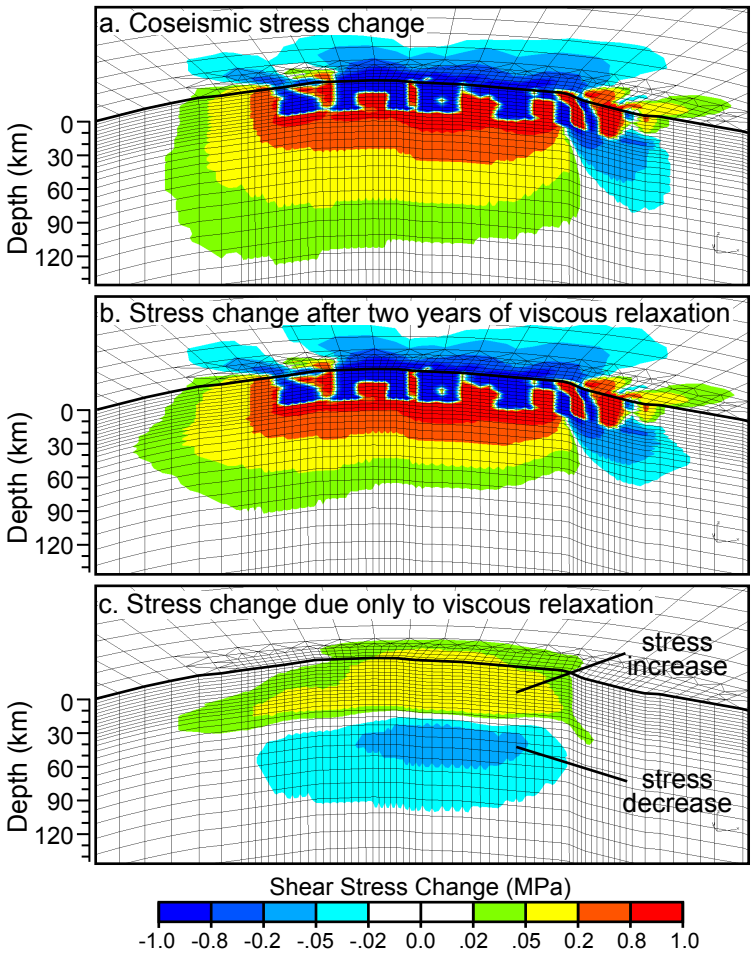

Freed et al., Figure 12

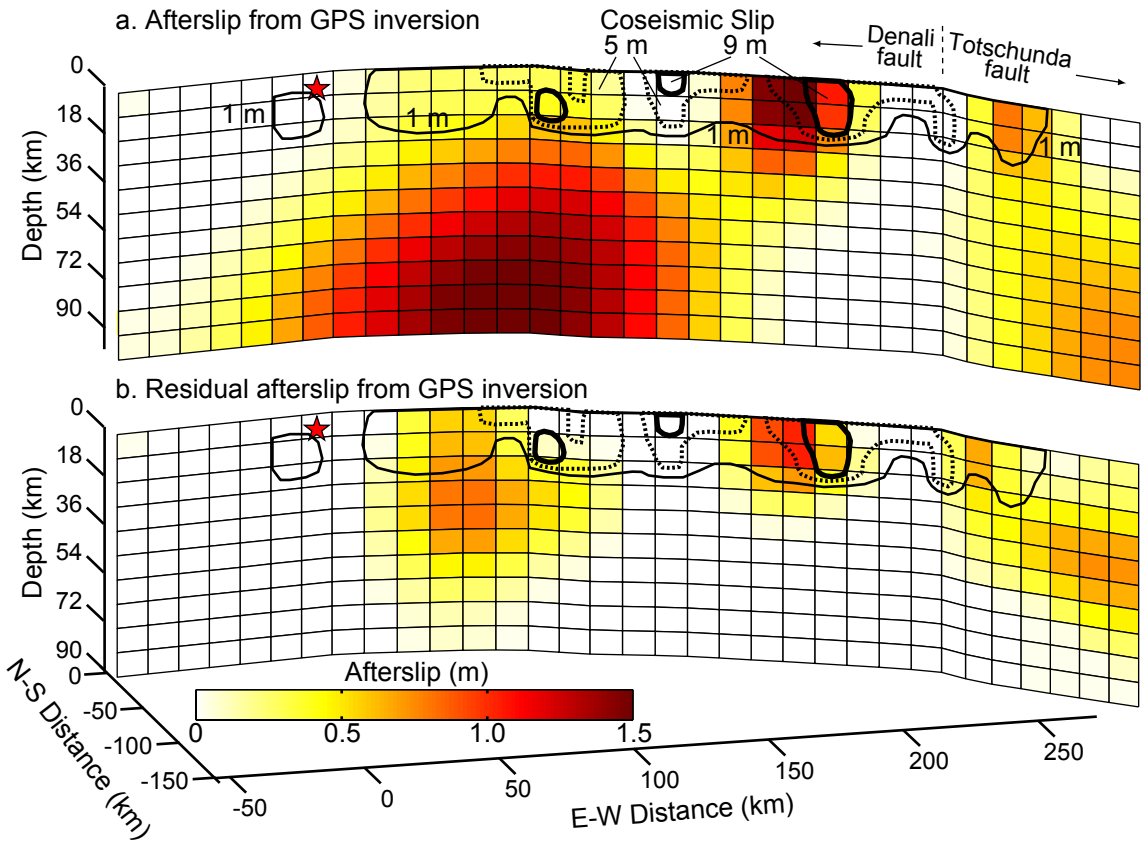

Freed et al. Figure 13

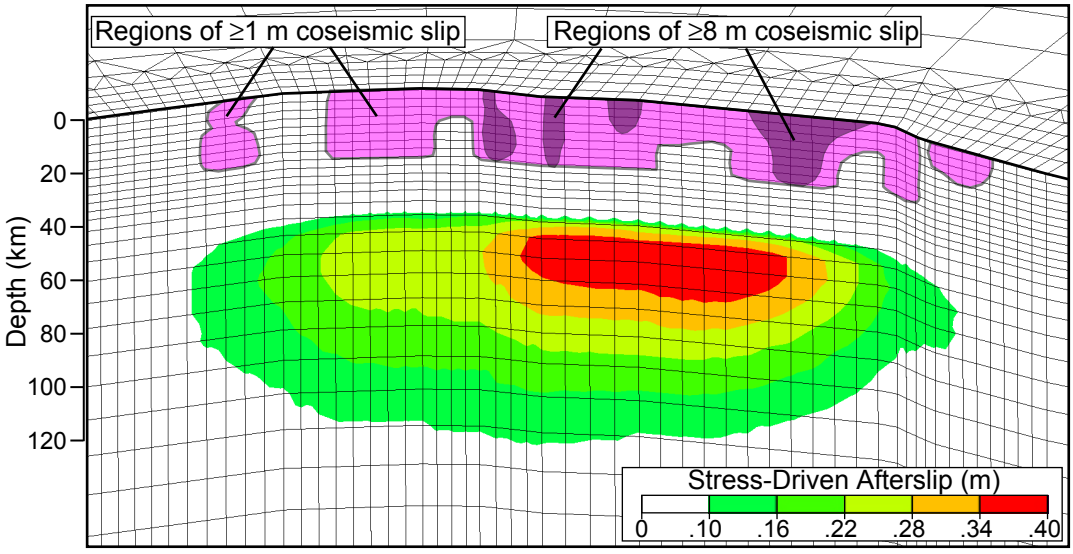

Freed et al., Figure 14

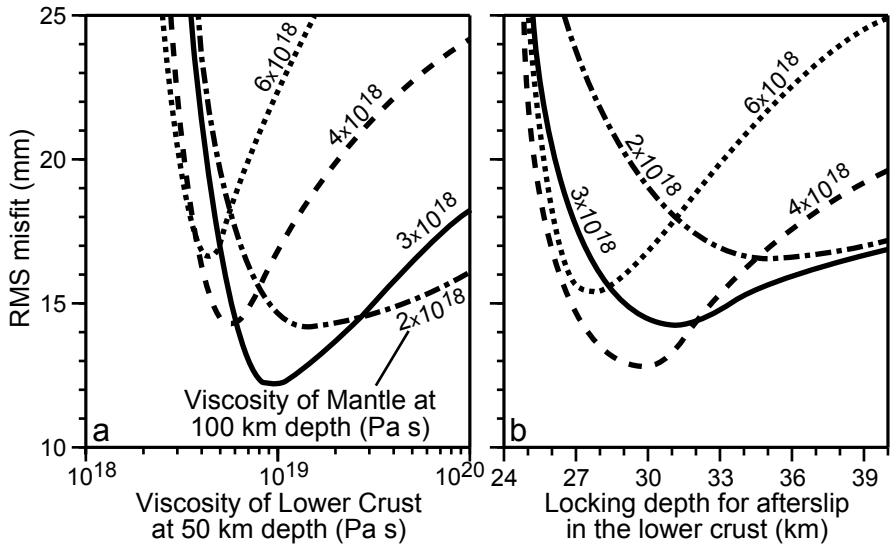

Freed et al., Figure 15

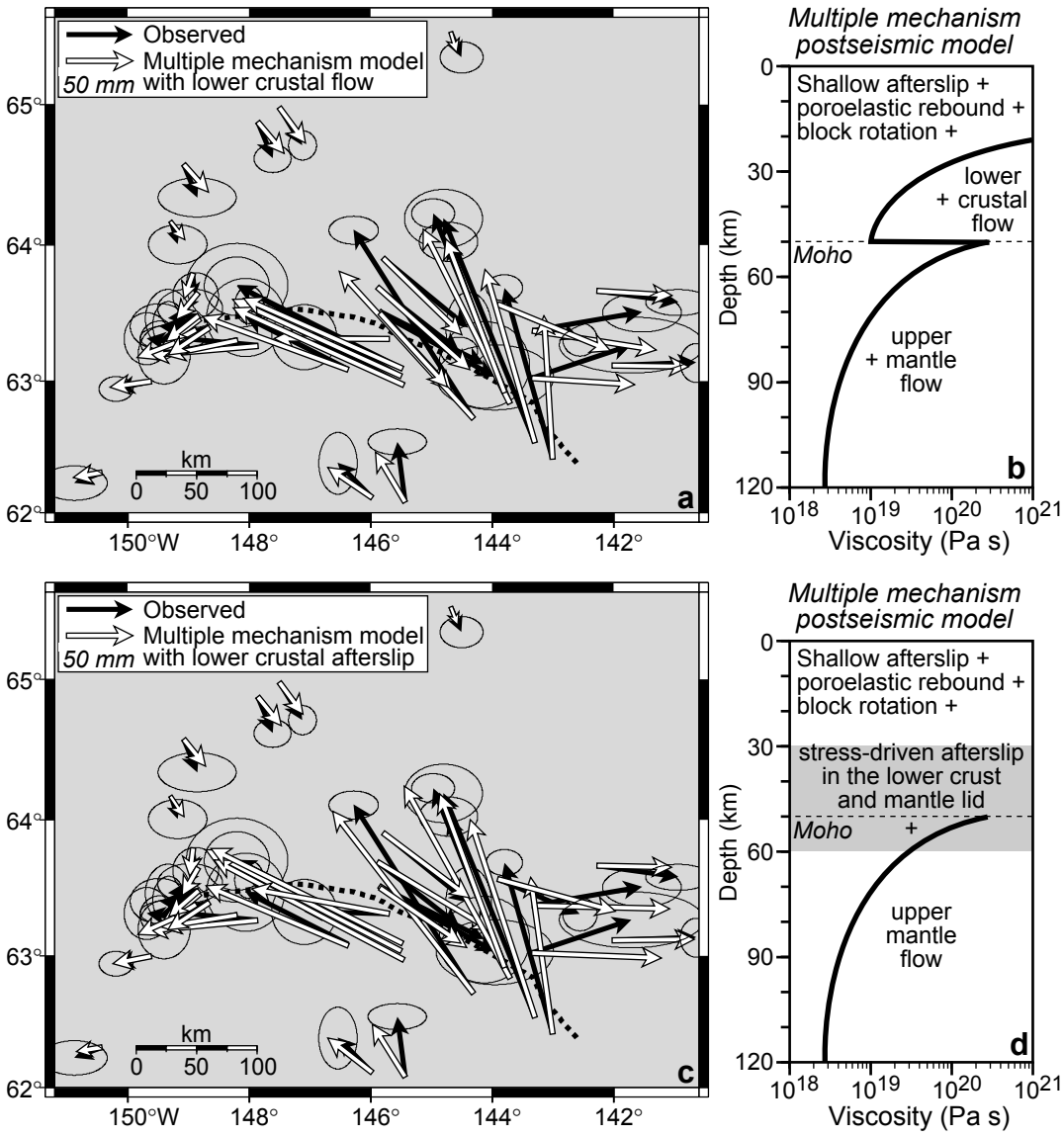

Freed et al. Figure 16

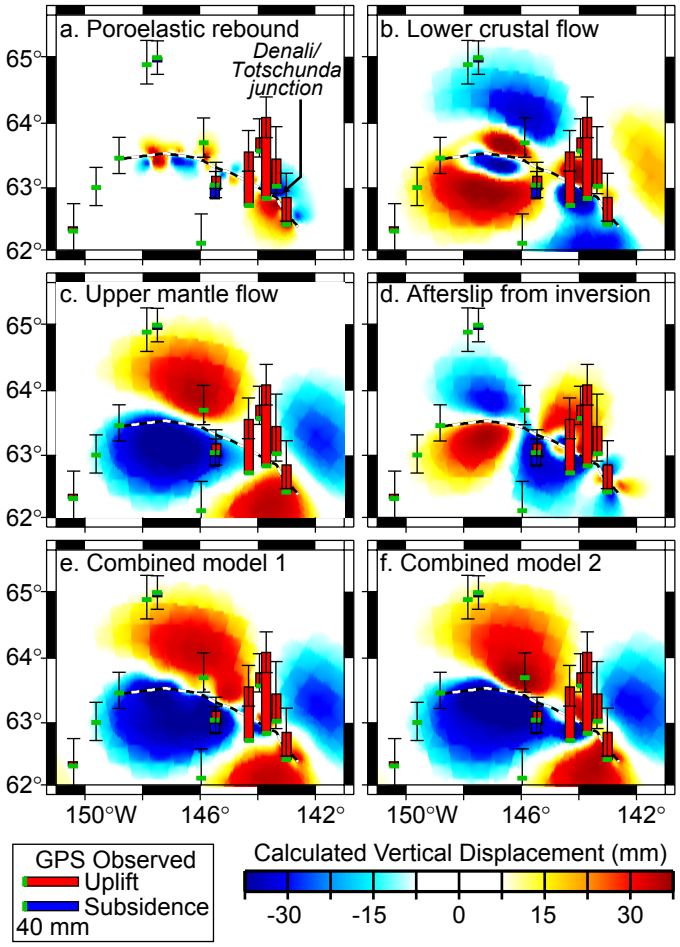

Freed et al., Figure 17